PAPER

Spectroscopic analysis of tungsten spectra in extreme-ultraviolet range of 10-480 Å observed from EAST tokamak with full tungsten divertor

To cite this article: Wenmin Zhang *et al* 2024 *Phys. Scr.* **99** 105609

Physica Scripta

PAPER

Spectroscopic analysis of tungsten spectra in extreme-ultraviolet range of 10-480 Å observed from EAST tokamak with full tungsten divertor

RECEIVED
20 June 2024

REVISED
29 August 2024

ACCEPTED FOR PUBLICATION
3 September 2024

PUBLISHED
12 September 2024

Wenmin Zhang[1,2], **Ling Zhang**[1], **Shigeru Morita**[3], **Yunxin Cheng**[1], **Fengling Zhang**[1,2], **Ailan Hu**[1], **Chengxi Zhou**[1], **Zhengwei Li**[1,4], **Yiming Cao**[1,4], **Jiuyang Ma**[1,2], **Darío Mitnik**[5], **Yinxian Jie**[1] and **Haiqing Liu**[1]

[1] Institute of Plasma Physics, Hefei Institutes of Physical Science. Chinese Academy of Sciences, Hefei 230031, People's Republic of China
[2] University of Science and Technology of China, Hefei 230026, People's Republic of China
[3] National Institute for Fusion Science, Toki 509-5292, Gifu, Japan
[4] Anhui University, Hefei 230601, People's Republic of China
[5] Instituto de Astronomíay Física del Espacio (CONICET-Universidad de Buenos Aires), Buenos Aires 1428, Argentina

E-mail: zhangling@ipp.ac.cn

Keywords: EAST plasma, tungsten burst, extreme ultraviolet spectra, tungsten lines

Abstract

Tungsten spectra in extreme ultraviolet (EUV) wavelength range of 10-480 Å have been observed from high-temperature plasmas in Experimental Advanced Superconducting Tokamak (EAST) with full tungsten divertor using four fast-time-response EUV spectrometers of EUV_Short (5-45 Å), EUV_Long_a (40–180 Å), EUV_Long_c (130–330 Å) and EUV_Long_b (270–480 Å) and two space-resolved EUV spectrometers of EUV_Short2_d (45–70 Å) and EUV_Long2_d (40–130 Å). The wavelength of measured spectra is accurately calibrated based on several well-known spectral lines emitted from low-Z (He, Li, C, N and O), medium-Z (Fe and Cu) and high-Z (Mo) impurity ions. Measurements of the tungsten spectra were taken from discharges accompanied with a transient tungsten burst event, which creates a pulsed influx of tungsten atoms into the EAST plasma. The tungsten spectra observed before and after the burst event are carefully analyzed with temporal behavior and radial profile distribution of the tungsten line intensity. As a result, 213 tungsten lines are successfully confirmed in the spectra observed after the tungsten burst, and the results are summarized in tables. These tungsten lines include line identifications of 78 lines of W XXIII - W XLVI (W^{22+} - W^{45+}) at 10–140 Å and 88 lines of W V - W IX (W^{4+} - W^{8+}) at 160–480 Å, while 47 tungsten lines at 50–380 Å could not be clarified the transition. In addition, quasi-continuum spectra called unresolved transition array (UTA) from tungsten ions in low- and high-ionization stages are also analyzed in three wavelength ranges of 18–38 Å, 45–70 Å and 150–280 Å at which W XXIII - W XXXVIII (W^{22+} - W^{37+}), W XXVII - W XLVI (W^{26+} - W^{45+}) and W VI—W IX (W^{5+} - W^{8+}) are dominantly emitted, respectively. Through the analysis it is found that charge state distributions of tungsten UTA at 140–220 Å significantly vary with decrease in the electron temperature. Ionization stages of all observed tungsten lines including both isolated and quasi-continuum lines are experimentally reconfirmed by comparing the radial intensity profile with the electron temperature profile. Finally, spectral lines useful for tungsten diagnostic in fusion plasmas are selected and marked in the tables.

1. Introduction

In International Thermonuclear Experimental Reactor (ITER) the thermal heat load on divertor plates is surprisingly large. Then, tungsten material was decided to use for the divertor plate, replacing carbon material which has been used for many years, because the tungsten material has high-melting point, high-physical sputtering threshold energy, low-tritium retention and low-dust production rate. At present, the tungsten

monoblock and tungsten-coated materials have been used in several tokamak devices, e.g. ASDEX Upgrade [1], JET [2], EAST [3] and WEST [4]. In ITER, very recently, the tungsten material was also decided to use for the first wall on the vacuum vessel. It is well-known that high-Z element like tungsten easily lowers the plasma temperature and degrades the plasma performance due to the huge radiation rate once it enters the plasma as an impurity ion. Therefore, diagnostic of the tungsten atom/ions is more important than ever before because of the inevitable importance of protecting the plasma from tungsten contamination for steady sustainment of high-performance plasma. Since the electron temperature of ITER plasmas is extremely high, e.g. several tens keV, a variety of charge stages of tungsten ions exist in the ITER plasma, i.e. from neutral tungsten atoms (W^0) at the divertor to He-like tungsten ions (W^{72+}) at plasma core.

So far, emission lines of the tungsten ions have been measured in various wavelength ranges of soft x-ray (SXR: 1–10 Å), extreme ultraviolet (EUV: 10–500 Å), vacuum ultraviolet (VUV: 500–3000 Å) and visible (3000–8000 Å) ranges using magnetic confinement devices for fusion research [5–19], electron-beam ion trap (EBIT) for atomic physics study [20–23] and sliding-spark light discharges for laboratory plasma study [24–28].

A neutral tungsten emission line of W I has been identified as an isolated line with transition of $5d^5 6s\ ^7S_3$–$5d^4 6s6p\ ^7P^\circ_4$ in the visible range of 4009 Å [11]. The emission line with relatively strong intensity is now an important experimental tool for plasma-wall interaction study of in fusion research. Line emissions of W III - W VII from low-ionized tungsten ions have been found in the VUV wavelength range of 495–1475 Å by injecting a coaxial tungsten pellet on large helical device (LHD) [12]. Spectral lines of W VII were also observed from the SSPX spheromak in the EUV wavelength range of 180–450 Å using a flat-field spectrometer with spectral resolution of 0.3 Å [7]. In both VUV and EUV wavelength ranges of 150–1480 Å tungsten spectra of W IV - W VIII observed from JET tokamak were analyzed in detail [29]. Ryabtsev *et al* accurately identified numerous tungsten spectral lines of W VIII - W IX observed from vacuum spark plasma in the EUV wavelength range of 160–271 Å using a grazing-incidence spectrometer with 3600 lines/mm grating [28]. These results made a significant contribution to fill in missing experimental data for low-ionized tungsten ions. Nineteen tungsten lines of W V, W VII and W VIII were also found in both VUV and EUV ranges of 160–500 Å in LHD [13]. The spectral feature of these lines, in particular, W VII and W VIII, was quite different from those observed in SSPX, JET and EBIT devices. The reason may be due to entirely different electron density ranges among four devices. Two isolated strong W VII lines with transitions of $4f^{14}5s^2 5p^6\ ^1S_0$—$4f^{14}5s^2 5p^5 5d$ emitted in the EUV wavelength range of 216.219 Å and 261.387 Å were found at a tungsten burst phase after accumulated laser blow-off (LBO) experiments in the HL-2A tokamak. The spectral feature of these two W VII lines was quite similar to those from SSPX and JET. The tungsten influx rate in the HL-2A discharge was analyzed using the W VII line and studied tungsten behavior at the plasma edge [14].

In addition to the above, highly ionized tungsten ions, e.g. W^{27+} - W^{50+}, have been further studied extensively. Tungsten lines of W XXXVIII - W LI (W^{37+} - W^{50+}) observed from ASDEX Upgrade by mean of LBO technique were identified in the SXR wavelength range of 5–15 Å [6]. Tungsten lines of W XLVI (W^{45+}) and W XLVII (W^{46+}) observed from JET using an upgrade high-resolution x-ray spectrometer in the SXR wavelength range of 5.20–5.24 Å were identified as 3p-4d inner-shell excitation lines [30]. Tungsten lines of W XLVII (W^{46+}) were also observed in LHD in the SXR wavelength range of 7–8 Å and 7.938 Å by injecting a tungsten pellet [15].

In the EUV wavelength range, on the other hand, the presence of quasi-continuum spectrum called unresolved transition array (UTA) is particularly emphasized, while several isolated spectral lines from highly ionized tungsten ions, e.g. W XLI - W XLVI (W^{40+} - W^{45+}), have been measured in the EUV wavelength range in several EBIT [31, 32] and fusion devices [6, 13, 15, 18]. The UTA spectra basically originate in a large relativistic effect of the high-Z element, e.g. level mixing due to spin–orbit interaction. The tungsten UTA spectra are mainly located in wavelength ranges of 15–40 Å, 45–56 Å and 56–75 Å. A typical feature of the UTA spectrum is that the shape greatly varies with electron temperature. For example, the shape of the UTA at 15–40 Å wavelength range mainly composed of W^{22+} - W^{37+} ions [9, 11, 33, 34] largely shifts the peak intensity position when the electron temperature increases from 0.75 keV to 1.0 keV. Radial profiles of such UTA spectra have been measured using a space-resolved EUV spectrometer in LHD and densities of W^{24+}, W^{25+} and W^{26+} ions are evaluated at 32.16–33.32 Å, 30.69–31.71 Å and 29.47–30.47 Å by analyzing the radial profile, respectively [35].

In the high-Z element intensities of magnetic dipole (M1) forbidden transitions become sufficiently strong due to an entire breaking of L-S coupling, e.g. M1 transition rate increases with Z^{10}, while E1 transition rate increases with Z^4 [36]. The M1 transitions have been observed in LHD for W XXVII - W XXVIII (W^{26+}-W^{27+}) in the visible wavelength range of 3300–3900 Å and W XXX - W XL (W^{29+}-W^{39+}) in the VUV wavelength range of 500–900 Å [16, 37, 38]. The visible M1 transition is useful for tungsten diagnostic of ITER because use of the optical fiber and/or mirror enables visible spectroscopy in the absence of strong neutron and hard x-ray backgrounds.

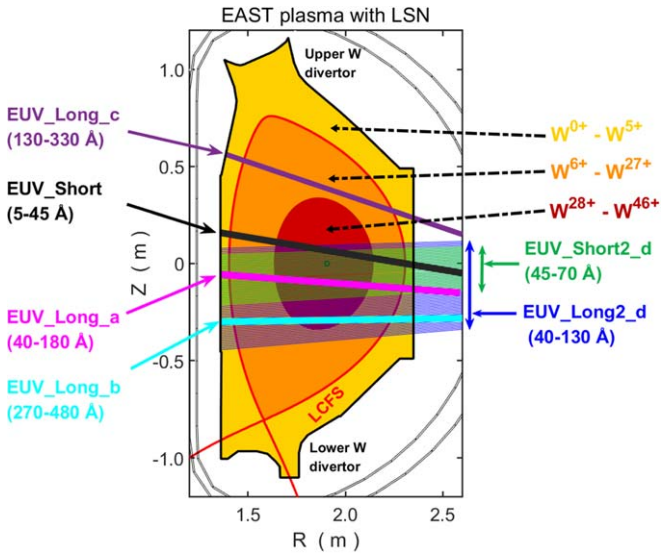

Figure 1. Poloidal cross section of EAST tokamak with lower single null configuration. Vertical and horizontal axes mean vertical distance from equator plane and horizontal distance from torus center (major radius), respectively. Plasma boundary defined with Last Closed Flux Surface (LCFS) is shown in solid red line. Lines-of-sights (LOS) of four fast-time-response EUV spectrometers are indicated with thick solid lines (EUV_Long_c: purple, EUV_Short: black, EUV_Long_a: pink, and EUV_Long_b: cyan). Vertical observation ranges of two space-resolved EUV spectrometers are indicated with shaded area (EUV_Long2_d: blue and EUV_Short2_d: green). Vertical observation size of the LOS is different for each fast-time-response EUV spectrometer (EUV_Long_c: 120 mm, EUV_Short: 200 mm, EUV_Long_a: 200 mm and EUV_Long_b: 200 mm), and horizontal observation size is roughly 50 mm for all of them. For an easy understanding of EAST tokamak plasma, the D-shaped plasma area within the LCFS is simply categorized by two different temperature regions of edge plasma region (orange-filled area) and core plasma region (red-filled area), where tungsten ions of W^{6+} - W^{27+} (ionization energy: $E_i = 122–1132$ eV) and W^{28+} - W^{46+} ($E_i = 1132–4180$ eV) are localized when central electron temperature is 4.5 keV, respectively. Tungsten atoms/ions of W^{0+} - W^{5+} ($E_i = 8–122$ eV) are localized in scrape-off layer and divertor region outside the LCFS denoted with yellow-filled area.

This work focuses on observations of the tungsten emission lines in EAST discharges over the entire EUV wavelength range of 10–480 Å and analyses of the tungsten spectra. The observations have been carried out with four fast-time-response EUV spectrometers of EUV_Short, EUV_Long_a, EUV_Long_c and EUV_Long_b working in wavelength ranges of 5–45 Å, 40–180 Å, 130–330 Å and 270–480 Å, respectively, and two space-resolved EUV spectrometers of EUV_Short2_d and EUV_Long2_d working in wavelength ranges of 45–70 Å and 40–130 Å, respectively. Temporal behaviors and radial profiles of the tungsten emission lines are utilized for the accurate analysis of tungsten spectral lines. To analyze accurately the temporal behavior of tungsten ion a spontaneous tungsten burst event appeared during a discharge is used. In such discharges the tungsten influx suddenly increases due to an enhanced plasma-wall interaction. Based on the burst event time differences in spectral appearance can be clearly observed among spectral lines from different tungsten ionization stages. As a result, several emission lines from low-ionized tungsten ions are found in EUV spectra at the wavelength range of 150–480 Å observed from EAST plasmas.

In the present paper, experimental setup is explained in chapter 2 with installed four fast-time-response and two space-resolved EUV spectrometers. Results on spectroscopic analyses of measured tungsten emission lines are presented in chapter 3 including tungsten UTA spectra and emission lines from low-ionized tungsten ions. Identified tungsten lines are summarized in tables. Transitions of several tungsten emission lines observed here were unfortunately unknown. In chapter 4 unknown tungsten emission lines are discussed in finding their possible ionization stages through analyses of the temporal behavior and radial profile. Results are also summarized in tables. Finally, the present work is summarized in chapter 5.

2. Experimental setup

The EAST is a medium-sized superconducting tokamak (major radius of $R = 1.85$ m at the plasma center, averaged minor radius of $a = 0.45$ m at the plasma edge boundary and toroidal magnetic field of $B_t = 3.5$ T), and creates high-temperature toroidal plasma with D-shaped poloidal plasma cross section, as shown in figure 1. To make an easy understanding of EAST tokamak plasma the D-shaped plasma area within the last closed flux surface (LCFS) is simply categorized by two different temperature regions of the edge plasma region (orange-filled area) and the core plasma region (red-filled area), where tungsten ions of W^{6+} - W^{27+} (ionization energy: $E_i = 122–1132$ eV) and W^{28+} - W^{46+} ($E_i = 1132–4180$ eV) are localized, respectively, when

central electron temperature is 4.5 keV. Tungsten atoms/ions of W^{0+} - W^{5+} ($E_i = 8$–122 eV) are localized in the scrape-off layer and divertor region indicated with yellow-filled area. The line-averaged electron density (n_e) and electron temperature (T_e) in EAST discharges range in $n_e \leqslant 7 \times 10^{19}$ m^{-3} and $T_e \leqslant 12$ keV, respectively [39]. The first wall of the vacuum chamber is mainly formed of molybdenum tiles. Replacement of graphite divertor plates by tungsten divertor plates (tungsten-copper monoblocks) was completed in 2021 for both upper and lower divertor regions. Molybdenum material is partly used for the first wall on the inboard side vacuum vessel. Iron and copper materials are used for protection of Ion-Cyclotron-Range-of-Heating (ICRH) antennas [40].

In EAST two fast-time-response EUV spectrometers (EUV_Long_a: 20–500 Å and EUV_Short: 5–138 Å) are installed for monitoring impurity behavior in the core plasma and other two fast-time-response EUV spectrometers (EUV_Long_c: 20–500 Å and EUV_Long_b: 20–500 Å) are installed for monitoring impurity behavior in the edge plasma [40, 41]. Two types of the spectrometers named 'EUV_Long' and 'EUV_Short' use holographic gratings with different number of grooves, i.e. 'EUV_Long' for 1200 grooves/mm and 'EUV_Short' for 2400 grooves/mm. Therefore, 'EUV_Short' has better spectral resolution in short wavelength range below 50 Å, while the spectrometer throughput is extremely low in longer wavelength range above 100 Å. The line-of-sights (LOS) of these spectrometers are shown in figure 1. EUV spectra from the fast-time-response spectrometers can be recorded every 5 ms using a back-illuminated charge-coupled detector (CCD: 26×26 μm^2/pixel, 1024×255 pixels and 26.6×6.6 mm^2) operated in Full Vertical Binning (FVB) mode. The wavelength range to be measured can be externally changed by moving the CCD position horizontally along the focal plane with an electric pulse motor equipped on the spectrometer. Observation range at the plasma center in the vertical direction is roughly 120 mm for EUV_Long_c and 200 mm for EUV_Short, EUV_Long_a and EUV_Long_b, while that in the horizontal (or toroidal) direction takes the same value of 50 mm for all spectrometers. In this work the wavelength ranges of EUV_short, EUV_Long_a, and EUV_Long_c and EUV_Long_b spectrometers are set to 5–45 Å, 40–180 Å, 130–330 Å and 270–480 Å, respectively, to observe wider wavelength range in a single discharge.

In EAST, on the other hand, two space-resolved EUV spectrometers called EUV_Short2_d and EUV_Long2_d equipped with a space-resolved slit are installed for spatial distribution measurement of impurity line emissions in the wavelength ranges of 5–138 Å and 30–520 Å, respectively [19, 42]. A complementary metal-oxide semiconductor (CMOS: 6.5×6.5 μm^2/pixel, 2048×2048 pixels and 13.3×13.3 mm^2) detector is used for EUV_Short2_d spectrometer to increase the time response in recording the spectral image, while the CCD (26.6×6.6 mm^2) detector, same as the fast-time-response spectrometer case, is used for EUV_Long2_d spectrometer by arranging the CCD vertically. Then, the vertical observation range is different between EUV_Short2_d and EUV_Long2_d, i.e. -18 cm $\leqslant Z \leqslant 8$ cm ($0 \leqslant r/a \leqslant 0.3$) for EUV_Short2_d and -40 cm $\leqslant Z \leqslant 10$ cm ($0 \leqslant r/a \leqslant 0.7$) for EUV_Long2_d. Here, r and a are the poloidally-averaged radial position and radial plasma size, respectively. Therefore, values of $r/a = 0$ and 1 mean the plasma center and edge boundary, respectively. The plasma edge boundary is defined by the LCFS as seen in figure 1. It is noted that the wavelength range of EUV_Long2_d with CCD which can be simultaneously measured in a single discharge, $\Delta\lambda_{WR}$, is much narrower than 'EUV_Long' with CCD, e.g., $\Delta\lambda_{WR} = 30$ Å at $\lambda_0 = 60$ Å, because the short axis (6.6 mm) of CCD is set along the horizontal wavelength dispersion.

The wavelength calibration of four fast-time-response EUV spectrometers is performed using two methods based on theoretical prediction calculated from spectrometer dispersion equation and CCD pixel positions of experimentally observed impurity spectral lines. In EAST discharges intrinsically existing several impurity species can be found such as He, Li, C, N, O, Fe, Cu, Mo and W. The impurities of He and Li originate in glow discharge and lithium coating for wall conditioning, respectively, and N and O originate from a small air leakage of the vacuum vessel and water vapor in the vacuum vessel, respectively. In main discharges with heating systems, several metallic impurities such as Fe, Cu, Mo and W are contaminated in plasmas due to an interaction with plasma facing components. In radiofrequency (RF) wave heating antennas and guard limiter interact with particles accelerated by the heating wave, when the RF wave does not couple effectively to the edge plasma. High-energy particles accelerated by the heating waves interact with first wall, when those particles deviate from LCFS. In neutral beam injection the high-energy beam penetrates the plasma in low-density discharges and interacts with first wall. The neutral beam may also interact with plasma facing components around the injection port due to the beam divergence effect. Figure 2 shows the EUV spectra measured for the wavelength calibration. The spectral lines were analyzed and identified in the wavelength range of 10–480 Å [40, 43, 44]. The wavelengths denoted in the figures are taken from National Institute of Standards and Technology (NIST) database [45].

In figure 2(a), $n = 3$-2 L_α transitions of Cu XX—Cu XXI and Fe XVII—Fe XVIII mainly contribute to the spectrum formation in the wavelength ranges of 10–13 Å and 15–18 Å, respectively, whereas no impurity lines appear in the wavelength range of 5–10 Å. Spectral lines emitted in the wavelength range of 18–45 Å are mainly composed of H- and He-like C, N and O ions with resonance series transitions of np-1s ($n = 2$ and 3). In

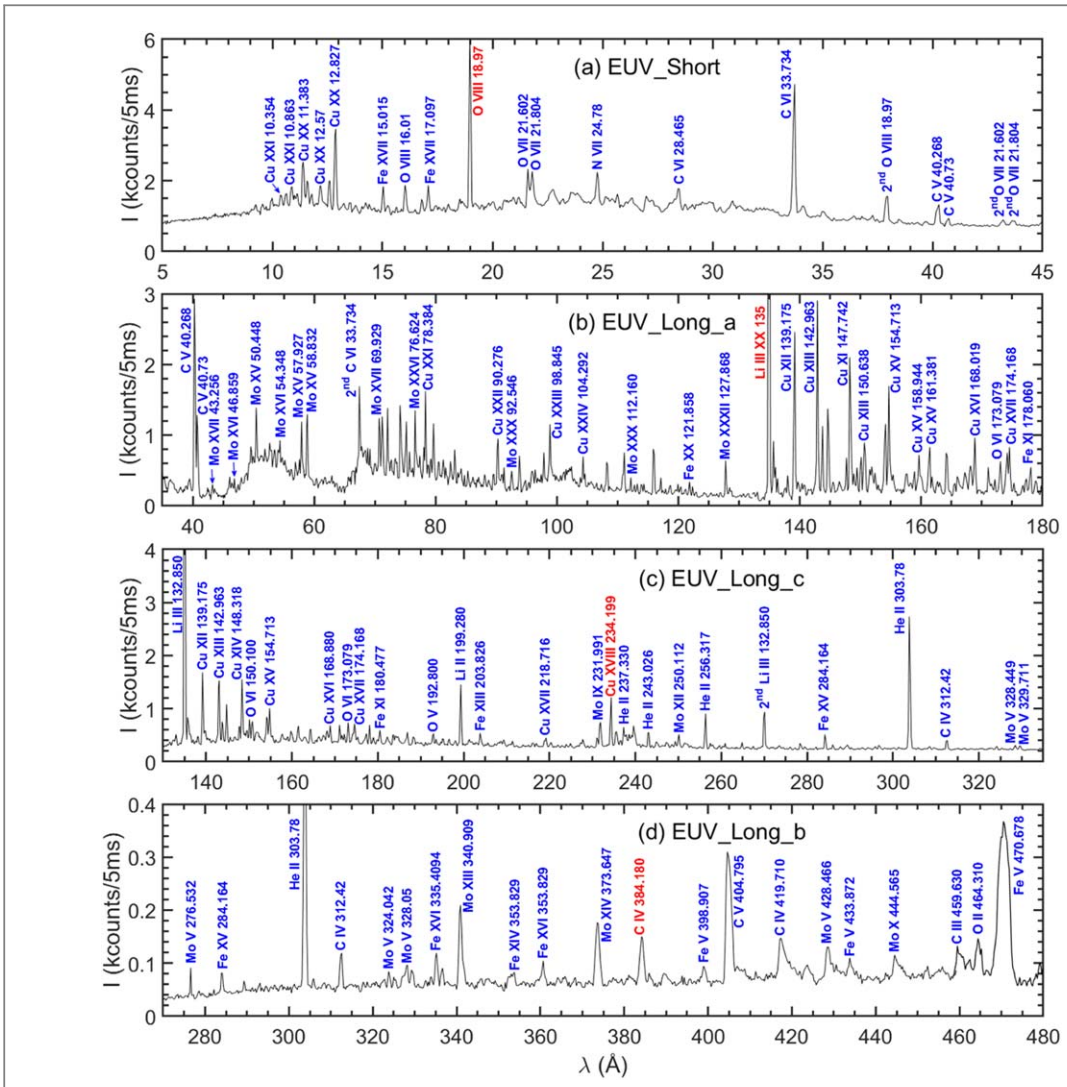

Figure 2. Well-known EUV spectral lines for wavelength calibration in wavelength range of 5–480 Å; (a) 5–45 Å (EUV_Short), (b) 40–180 Å (EUV_Long_a), (c) 130–330 Å (EUV_Long_c), and (d) 270–480 Å (EUV_Long_b). Each spectrum is observed at different discharges. Spectral resolution becomes quickly worse above 400 Å due to increased discrepancy between focal plane and linear detector position. Spectral lines indicated with red color are used for determination of absolute position in theoretical wavelength calibration.

figure 2(b) it is seen that a large number of Cu, Mo and W lines are very closely emitted in the wavelength range of 40–180 Å. In the present wavelength calibration, the line identification of Cu and Mo spectra are important. In particular, Cu XI - Cu XIX from low-ionized Cu ions at 139–180 Å, Cu XXI - Cu XXVI from highly ionized Cu ions with n = 2-2 transitions at 75–135 Å, Mo V - Mo XVII from low-ionized Mo ions at 42–70 Å, 225–260 Å and 320–380 Å, and Mo XXIV - Mo XXXII from highly ionized Mo ions at 70–95 Å and 104–130 Å are useful, as shown in figures 2(b)–(d). Several emission lines of He II, C III-V and Fe V-XVI are also clearly seen in the long wavelength range of 235–480 Å.

For the theoretical wavelength calibration based on the dispersion equation reflecting the present spectrometer geometry a single well-known spectral line (see red lines in figure 2) is selected for each spectrum of figure 2 to determine the absolute value of the wavelength position. Here, we call it as theoretically calculated wavelength, λ_{cal}. Next, for the full experimental calibration, a cubic polynomial fitting is performed using several well-known spectral lines denoted with blue and red lines in figure 2. Here, we call it as experimentally determined wavelength, λ_{exp}.

Results of the wavelength calibration are shown in figure 3 for EUV_Short, EUV_Long_a, EUV_Long_c and EUV_Long_b. The values of X_0 mean a distance from the grating center to #1 CCD pixel position. Therefore, the wavelength range of $\Delta\lambda_{WR}$ is a function of X_0, i.e. $X_0 = 12$ mm (EUV_Short): 5–45 Å, 6 mm (EUV_Long_a): 40–180 Å, 25 mm (EUV_Long_c): 130–330 Å and 40 mm (EUV_Long_b): 270–480 Å. In the plot of EUV_Short in figure 3 there are no experimental values in the first 300 pixels, which correspond to the wavelength range of 2–10 Å, due to the absence of spectral lines as shown in figure 2(a).

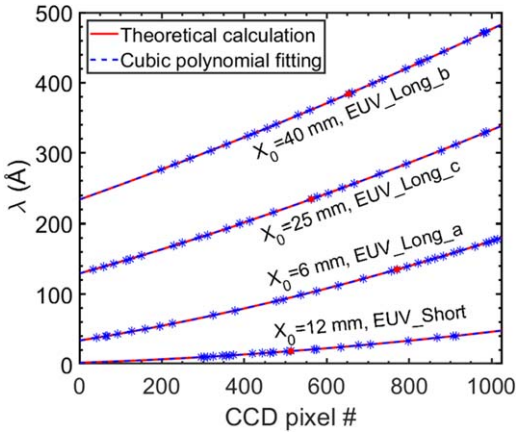

Figure 3. Wavelength calibrations based on theoretical calculation (method 1: red solid line, λ_{cal}) and cubic polynomial fitting among experimental values (method 2: blue dashed line, $\lambda_{fitting}$) for EUV_Short ($X_0 = 12$ mm: 5–45 Å), EUV_Long_a ($X_0 = 6$ mm: 40–180 Å), EUV_Long_c ($X_0 = 25$ mm: 130–330 Å), and EUV_Long_b ($X_0 = 40$ mm: 270–480 Å). Emission lines used for methods 1 and 2 are indicated by red solid circles and blue stars, respectively. Value of X_0 means distance from grating center to #1 CCD pixel position.

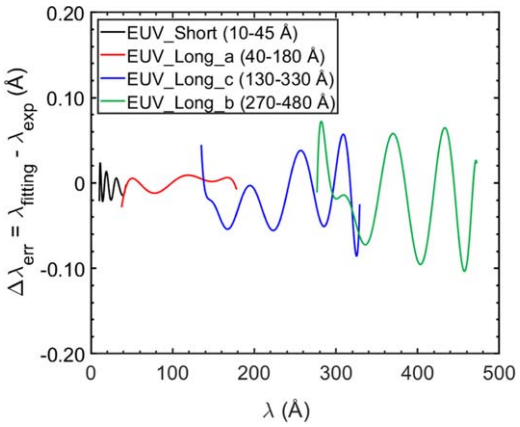

Figure 4. Uncertainties in wavelength calibration for four EUV spectrometers. Vertical axis, $\Delta\lambda_{err}$, indicates difference between cubic polynomial fitting values, $\lambda_{fitting}$, and experimental values, λ_{exp}.

The wavelength calibration curves plotted in figure 3 are in good agreement between the theoretical calculation denoted with red solid curve and the experimental calibration (cubic polynomial fitting) denoted with blue dashed curve. It means the position of optical components, in particular, the grating position, is placed precisely according to the designed values in the present spectrometer systems. It should be noted that, in figure 3, the theoretical calculation values for the EUV_Long_a, EUV_Long_b, and EUV_Long_c spectrometers are calibrated based on the experimental reciprocal linear dispersion of the gratings. This causes a difference in the wavelength calibration at overlapping ranges due to the nonlinearity of the grating dispersion based on a small deviation from theoretically determined value to each spectrometer component [41]. Then, the error in the present wavelength determination, i.e. wavelength uncertainty, can be estimated from the difference between wavelengths estimated from cubic polynomial fitting ($\lambda_{fitting}$) and wavelengths determined from well-known impurity lines (λ_{exp}), i.e. $\Delta\lambda_{err} = \lambda_{fitting} - \lambda_{exp}$. The result is shown in figure 4. It is found that the values of $\Delta\lambda_{err}$ are sufficiently small, i.e. $|\Delta\lambda_{err}| < 0.03$ Å for EUV_Short and EUV_Long_a, and $|\Delta\lambda_{err}| < 0.11$ Å for EUV_Long_c and EUV_Long_b.

In this study, other important diagnostics are also used for the data analysis, e.g. the line-averaged density, n_e, from polarimeter-interferometer (POINT) system [46], the electron temperature, T_e, and electron temperature profiles, $T_e(r/a)$, from 32-channel heterodyne radiometer system (ECE) [47], and the radiation loss from fast-response bolometers (central chord at Core I_{AXUV} and edge chord at Edge I_{AXUV}) [48]. Detailed explanations on the diagnostics are seen in each reference.

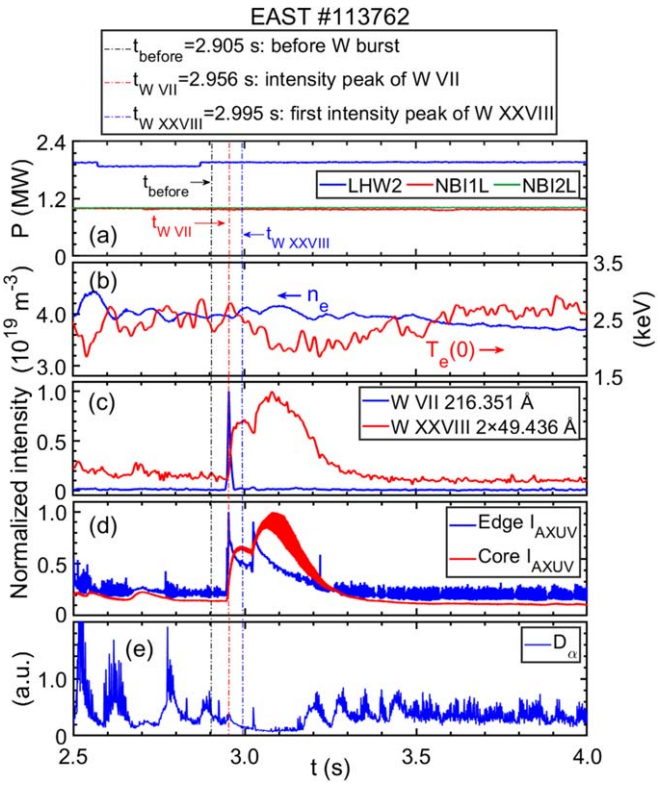

Figure 5. Typical waveform of #113762 discharge shot with sudden tungsten burst; (a) heating power of 4.6 GHz lower-hybrid wave (P_{LHW}: LHW2) and neutral beams (P_{NBI1L}: NBI1L and P_{NBI2L}: NBI2L), (b) line-averaged electron density (n_e) and central electron temperature ($T_e(0)$), (c) normalized tungsten line intensities (W VII: 216.351 Å, W XXVIII: 2 × 49.436 Å), (d) normalized radiation power (edge chord: Edge I_{AXUV}, central chord: Core I_{AXUV}) and (e) upper divertor D_α emission. The tungsten line intensity and radiation power are normalized at peak values. Vertical dash-dotted lines at t = 2.905 s, 2.956 s, and 2.995 s denote timings before tungsten burst, intensity peak of W VII and first intensity peak of W XXVIII, respectively, at which three EUV spectra are plotted in figure 7.

3. Analysis and identification of tungsten spectra

A typical EAST discharge with tungsten burst (#113762: upper single-null (USN) configuration) is shown in figure 5. Line-averaged density of $n_e = 4.0 \times 10^{19}$ m^{-3} and central electron temperature of $T_e(0) \sim 2.5$ keV are sustained with additionally injected heating power from neutral beams with $P_{NBI} = 2.0$ MW and lower-hybrid wave with 4.6 GHz frequency of $P_{LHW} = 2.0$ MW. A sudden increase in the tungsten influx happens at t = 2.946 s. It is clearly seen in the temporal intensity behavior of W VII (216.351 Å) from low-ionized tungsten ions shown in figure 5(c). The W VII intensity has the maximum value at t = 2.956 s after 10 ms of the burst start (see red vertical dash-dotted line). The intensity of W XXVIII (2 × 49.436 Å: 2nd order) emitted from highly ionized tungsten ions existing in the plasma core region reaches the maximum value after 49 ms (t = 2.995 s) of the burst start (see blue vertical dash-dotted line).

These intensity behaviors on such low-ionized and highly ionized tungsten ions show a common impurity transport feature seen in every tokamak device after an external injection of impurity particles. For comparisons with the tungsten line intensity behavior, signals from absolute extreme ultraviolet photodiode (AXUV) array are plotted in figure 5(d) for the edge and core channels as Edge I_{AXUV} and Core I_{AXUV}, respectively. The time response of the Core I_{AXUV} signals is almost identical to the intensity behavior of W XXVIII, while a clear difference appears between the W VII and Edge I_{AXUV} signals. In this discharge a second tungsten burst seems to be appeared at t = 3.021 s (see Edge I_{AXUV}). However, the W VII intensity is unchanged. The reason may be related to a three-dimensional structure of the ELM burst at the plasma edge (see figure 5(e)). If the ELM burst happens on a tungsten plate toroidally far from the spectrometer observation position, it will be difficult to observe the emission from such low-charge state tungsten ions. In addition, we compared time evolutions of bulk radiated power and tungsten radiation before and after the tungsten burst (t = 2.90–3.20 s). The result shows that after the tungsten burst, the time evolution of tungsten radiation is consistent with changes in the bulk radiated power. Compared to other intrinsic impurity spectral lines (C, O, Fe, Cu, Mo), the tungsten line intensity after the tungsten burst increases 3 times higher that before the tungsten burst, while the other intrinsic impurity lines are almost no significant change. This indicates that the tungsten burst means a single tungsten

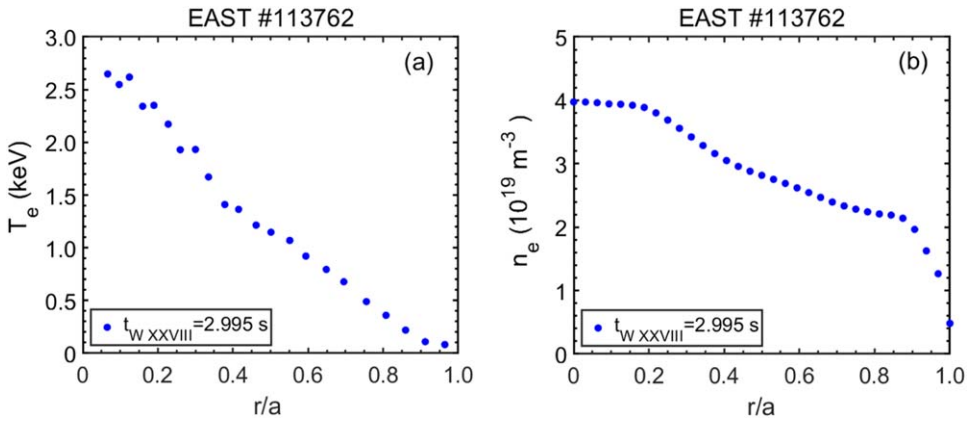

Figure 6. Radial profiles of (a) electron temperature measured by heterodyne radiometer (ECE) and (b) electron density measured by polarimeter interferometer (POINT) at t = 2.995 s in #113762 discharge. Horizontal axis means normalized minor radius (radial position of r is normalized by plasma minor radius of a = 0.450 m after conversion from D-shaped plasma to circular plasma). Then, values of r/a = 0 and 1 indicate plasma center and edge boundary defined by LCFS (see figure 1), respectively.

impurity sputtering event. In the present analysis, therefore, the first tungsten burst during t = 2.946 and 3.021 s is used for the identification of tungsten lines. A radial profile of the electron temperature measured with ECE and the electron density measured with POINT at $t_{W\ XXVIII}$ = 2.995 s is shown in figure 6 as a function of normalized plasma radius, r/a. As mentioned above, values of r/a = 0 and 1 mean the plasma center ($T_e(0) \sim 2.5$ keV) and plasma edge boundary ($T_e(1) \sim 0$), respectively. The temperature profile is necessary for detailed analysis of the tungsten spectra described in later section.

To accurately identify the tungsten spectral lines, three EUV spectra observed at different timings are selected, i.e. before, during and after the tungsten burst. The three spectra are plotted in figure 7 (before: t_{before} = 2.905 s in black color, during: $t_{W\ VII}$ = 2.956 s in red color and after: $t_{W\ XXVIII}$ = 2.995 s in blue color). These three timings are also indicated with vertical lines in figure 7. Figures 7(a)–(d) show EUV spectra measured with EUV_Short (5–40 Å), EUV_Long_a (40–130 Å), EUV_Long_c (130–330 Å) and EUV_Long_b (270–480 Å) spectrometers, respectively. Identified isolated lines are indicated in figure 7 for several impurity ions. It is obvious that the tungsten lines are emitted in different wavelength ranges depending on the ionization stage, e.g. low-ionized tungsten ions at 150–320 Å and highly ionized tungsten ions at 15–150 Å. The UTA spectrum at 45–70 Å during the tungsten burst plotted with blue solid line in figure 7(b) is totally saturated due to largely enhanced intensities. It is noticed here that the count rate of line emissions is less when the wavelength is longer, as shown in figures 7(b) and (d), because the throughput of the grazing-incidence spectrometer generally decreases with increasing wavelength. Therefore, the low count rate does not directly indicate weak intensity of the line emissions.

In this paper, the identified tungsten lines are indicated with green labels for W V - W XLVI (W^{4+} - W^{45+}) and line emissions from other impurities are indicated with black labels. In addition, unknown tungsten lines having no information on the transition are indicated with red labels. It should be noted that, based on other intrinsic impurity spectral lines identified in EAST discharges [40, 43, 44], i.e. He, Li, C, O, Al, Fe, Cu, Mo spectral lines, we carefully examined the overlapping of identified tungsten lines with other intrinsic impurity lines. Except for the overlapping of tungsten lines specifically noted in the manuscript, all other observed and identified lines are determined to be tungsten lines.

3.1. Identification of W XXIII - W XLVI from highly ionized tungsten ions

3.1.1. Tungsten UTA spectrum at 15–40 Å

Figure 8 shows tungsten spectra expanded to 15–40 Å of figure 7(a) measured at $T_e(0) \sim 2.5$ keV (see figure 6(a)). Since the relativistic effect becomes very large in high-Z elements such as Mo (Z = 42) and W (Z = 74), the quasi-continuum spectra like UTA can be always observed due to the overlapping of many line emissions at an extremely narrow wavelength interval. These tungsten lines can be analyzed with higher reliability by comparison with spectra from Compact Electron Beam Trap (CoBIT). Identified tungsten spectral lines shown in figure 8 are mainly composed of moderately ionized tungsten ions, i.e. W XXXIV - XXXVIII (W^{33+} - W^{37+}) at 18–25 Å, W XXVIII - XXXIV (W^{27+} - W^{33+}) at 25–29 Å and W XXIII - XXVII (W^{22+} - W^{26+}) at 29–40 Å.

The present identification of tungsten spectral lines can be also checked by comparing the temporal behavior of tungsten line intensities among different ionization stages of tungsten ions. The result is plotted in figure 9. The tungsten line intensity from low-ionized ions like W^{6+} quickly increases at t = 2.946 s just after the tungsten

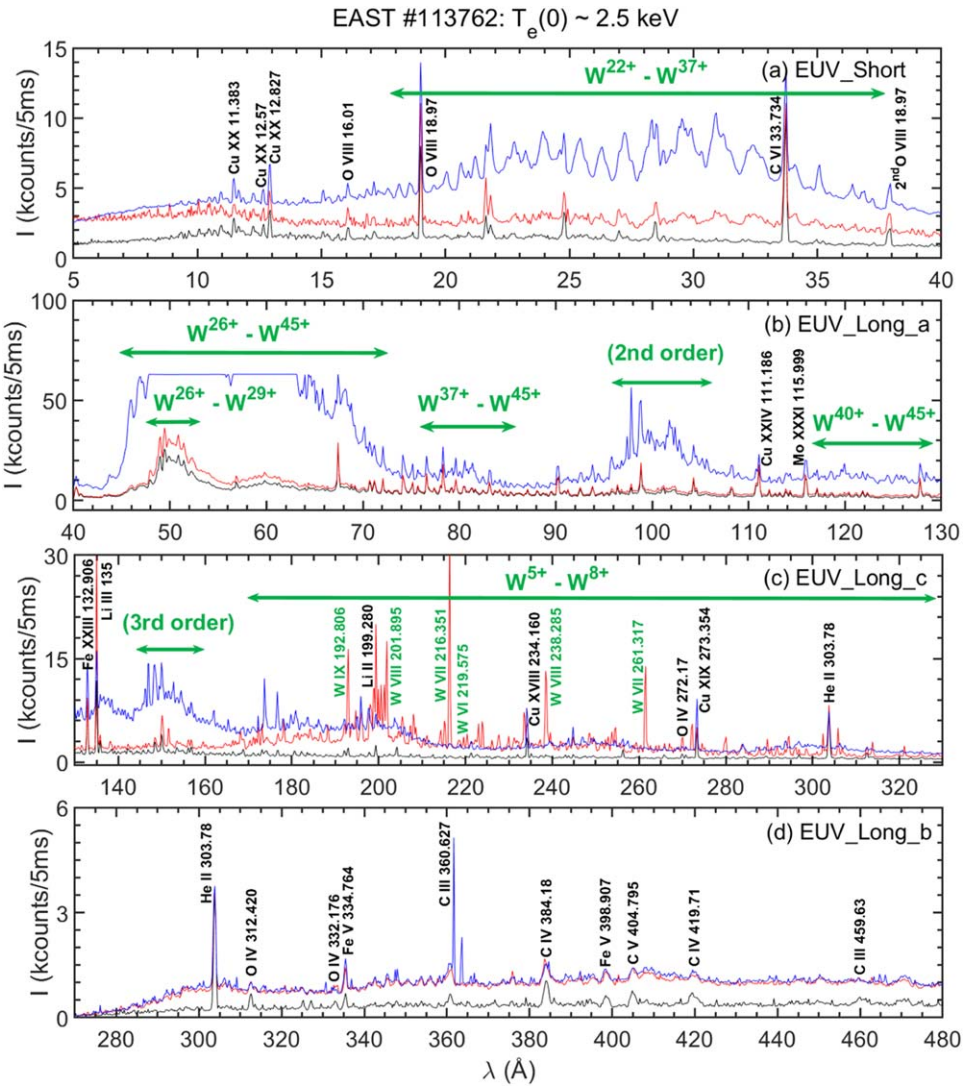

Figure 7. Three EUV spectra in wavelength ranges of (a) 5–40 Å (EUV_Short), (b) 40–130 Å (EUV_Long_a), (c) 130–330 Å (EUV_Long_c) and (d) 270–480 Å (EUV_Long_b) observed at t = 2.905 s (before tungsten burst: black color), t = 2.956 s (intensity peak of W VII: red color) and t = 2.995 s (first intensity peak of W XXVIII: blue color) in EAST discharge #113762 with $T_e(0) \sim 2.5$ keV. Three discharge timings are indicated in figure 5 with vertical dash-dotted lines.

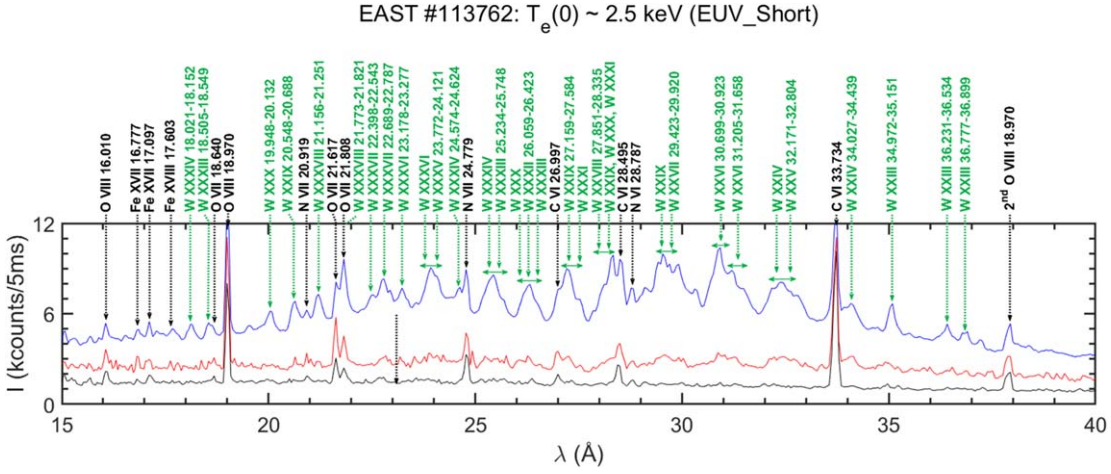

Figure 8. Enlarged tungsten spectra of figure 7(a) in wavelength range of 15–40 Å. Tungsten lines analyzed here as W XXIII - W XXXVIII (W^{22+} - W^{37+}) are denoted with green labels and lines from other impurity species are denoted with black labels. Discharge timings at which three spectra are observed are indicated in figure 5.

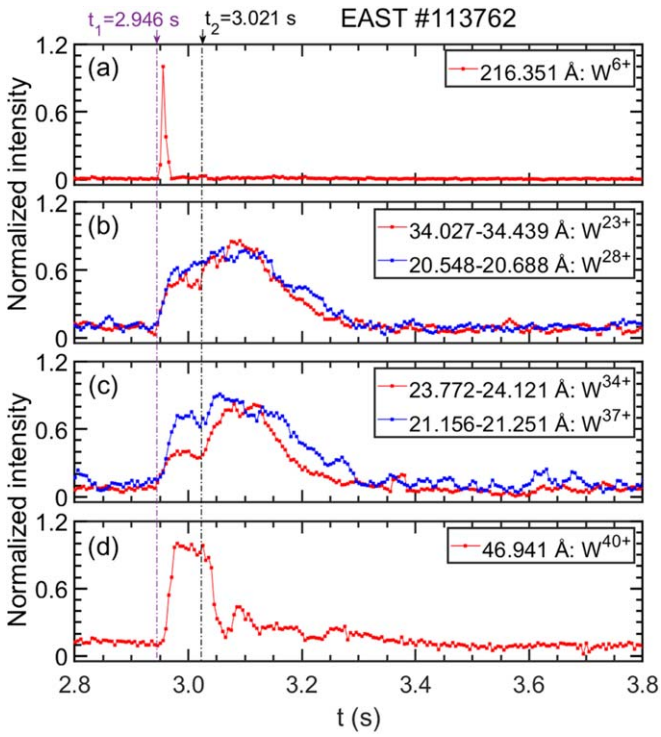

Figure 9. Time behaviors of tungsten line intensities at (a) 216.351 Å: W VII (W^{6+}) and at wavelength intervals of (b) 34.027–34.439 Å: W XXIV (W^{23+}) and 20.548–20.688 Å: W XXIX (W^{28+}), (c) 23.772–24.121 Å: W XXV (W^{34+}) and 21.156–21.251 Å: W XXXVIII (W^{37+}) and (d) 46.941 Å: W XLI (W^{40+}). Vertical dash-dotted lines at t = 2.946 s and 3.021 s indicate start and end of first W burst, respectively.

burst and disappears soon (see figure 9(a)). In contrast to this, the tungsten line intensity from moderately ionized tungsten ions gradually increases and remains a high level for a relatively long time until the end of the burst at t = 3.3 s (see figures 9(b) and (c)). In the case of highly-ionized tungsten ions like W^{40+}, on the other hand, the line intensity rapidly decreases at t = 3.021 s just after the second tungsten burst is triggered (see figure 9(d)). This is due to a sudden decrease in $T_e(0)$ from 2.5 to 1.9 keV (see figure 5(b)). Based on the tungsten UTA, tungsten densities of W^{26+}, W^{25+} and W^{24+} ions are evaluated in LHD at wavelength intervals of 29.47–30.47 Å, 30.69–31.71 Å and 31.16–33.32 Å [35].

The tungsten UTA lines at 15–40 Å identified in figure 8 are summarized in table 1. The tungsten lines of W XXIII—W XXXVIII (W^{22+} - W^{37+}), wavelengths from referenced database, intensities and transitions are listed with wavelengths and intensities observed in the present work. Some tungsten line transition data are not found in the references.

3.1.2. Tungsten UTA spectrum at 40–70 Å

As shown in figure 7(b), the EUV spectrum at 48–63 Å exceeded a saturation level (2^{16} = 65,536 counts/pixel) of the 16 bit CCD. Then, another discharge with higher electron temperature and lower tungsten concentration (EAST #103172: $T_e(0) = 4.5$ keV) was selected for analysis of the tungsten spectra in the wavelength range of 40–140 Å. The results are shown in figures 10(a) and (b) at wavelength ranges of 5–40 Å (EUV_Short) and 40–140 Å (EUV_Long_a), respectively. The spectra are taken at three different discharge timings similar to figure 7, i.e. before tungsten burst (t_{before} = 1.501 s: black lines), during tungsten burst ($t_{W\ VII}$ = 2.300 s at intensity peak of W VII: red lines), and after tungsten burst ($t_{W\ XXVIII}$ = 2.476 s at first intensity peak of W XXVIII: blue lines). A radial profile of the electron temperature measured with ECE and electron density measured with POINT at $t_{W\ XXVIII}$ = 2.476 s is shown in figure 11 as a function of normalized plasma radius, r/a. Values of r/a = 0 and 1 mean the plasma center ($T_e(0) = 4.5$ keV) and plasma edge boundary ($T_e(1) \sim 0$), respectively.

Results of the line identification in the wavelength range of 15–40 Å shown in figure 10(a) are totally consistent with the results from figure 8 despite the different electron temperatures between the two figures. On the contrary, the tungsten spectra are more complicated in the wavelength range of 45–70 Å as shown in figure 10(b). As reported in previous studies [5–11, 17, 33–35], the tungsten spectra are mainly composed of W^{24+} - W^{45+} ions. A simple spectral identification of the tungsten UTA is quite difficult due to the entire overlapping of tungsten spectra. Therefore, the EUV_Short2_d spectrometer (grating: 2400 grooves/mm) with

Table 1. Quasi-continuum lines (called UTA) of W XXIII - W XXXVIII (W^{22+} - W^{37+}) examined in the present work. First column shows tungsten lines. Second and third columns give minimum and maximum wavelengths, λ, determined in this work and taken from previously published data in the references, respectively. Intensities observed in this work and taken from previously published data are listed in fourth and fifth with minimum and maximum values, respectively. Label of '– – –' means the reference has no intensity information. Last two columns indicate lower and upper levels of the transition.

	λ (Å)				Intensities				Transitions	
W^{q+}	This work		Previous data		This work (10^{15} phs·m^{-2}·s^{-1}·Sr^{-1})		Previous data (a.u.)		Lower level	Upper level
	Min	Max	Min	Max	Min	Max	Min	Max		
W XXIII (W^{22+})	34.972 ± 0.01	35.151 ± 0.01		35.26 ± 0.02[a, b]	0.89	0.91	– – –	– – –	$4d^{10}4f^{6}$	$4d^{10}4f^{5}5g$
	36.231 ± 0.01	36.534 ± 0.01	36.2[c]	36.60 ± 0.04[b]	0.73	0.75	– – –	– – –	$4d^{10}4f^{6}$	$4d^{10}4f^{5}5g$
	36.777 ± 0.01	36.899 ± 0.01	35.5[d]	37[d]	0.68	0.70	– – –	– – –	$4d^{10}4f^{6}$	$4d^{10}4f^{5}5g$
W XXIV (W^{23+})	34.027 ± 0.01	34.439 ± 0.01	34.12 ± 0.06[a]		0.75	0.91	– – –	– – –	$4d^{10}4f^{5}$	$4d^{10}4f^{4}5g$
W XXV (W^{24+})	32.171 ± 0.01	32.804 ± 0.01	32.16–32.28[e]	32.63 ± 0.2[b]	0.93	1.06	3.38–4.18	– – –	$4d^{10}4f^{4}$	$4d^{10}4f^{3}5g$
W XXVI (W^{25+})	30.699 ± 0.01	30.923 ± 0.01	30.69–30.80[e]	30.90 ± 0.03[c]	1.23	1.36	3.38–3.88	– – –	$4d^{10}4f^{3}$	$4d^{10}4f^{2}5g$
	31.205 ± 0.01	31.658 ± 0.01	31.25–31.37[e]	31.59–31.71[e]	0.89	1.13	3.57–4.17	3.22	$4d^{10}4f^{3}$	$4d^{10}4f^{2}5g$
W XXVII (W^{26+})	29.423 ± 0.01	29.920 ± 0.01	29.47–29.58[e]	29.7 ± 0.1[a]	1.03	1.18	3.48–3.53	– – –	$4d^{10}4f^{2}$	$4d^{10}4f5g$
W XXVIII (W^{27+})	27.851 ± 0.01	28.335 ± 0.01	27.84–27.95[e]		0.69	1.24	– – –	– – –	$4d^{10}4f$	$4d^{10}5g$
W XXIX (W^{28+})	20.548 ± 0.01	20.688 ± 0.01		20.8 ± 0.1[a]	0.55	0.62	– – –	– – –	$4d^{10}$	$4d^{9}5f$
	27.159 ± 0.01	27.584 ± 0.01	27.20–27.30[e]	27.52–27.62[e]	0.76	0.97	2.64–3.42	1.82–2.32	$4d^{9}4f$	$4d^{9}5g$
W XXX (W^{29+})	19.948 ± 0.01	20.132 ± 0.01		20.2 ± 0.1[a]	0.49	0.55	– – –	– – –	$4d^{9}$	$4d^{8}5f$
W XXXII (W^{31+})	26.059 ± 0.01	26.423 ± 0.01	26.2 ± 0.1[a, d]	26.3[c]	0.73	0.84	– – –	– – –	$4d^{7}$	$4d^{6}5p$
W XXXIII (W^{32+})	18.505 ± 0.01	18.549 ± 0.01		18.6 ± 0.1[a]	0.38	0.41	– – –	– – –	$4d^{6}$	$4d^{5}5f$
	25.234 ± 0.01	25.748 ± 0.01	25.6 ± 0.1[a, d]	25.5[c]	0.71	0.88	– – –	– – –	$4d^{6}$	$4d^{5}5p$
W XXXIV (W^{33+})	18.021 ± 0.01	18.152 ± 0.01		18.1 ± 0.1[a]	0.36	0.40	– – –	– – –	$4d^{5}$	$4d^{4}5f$
	24.574 ± 0.02	24.624 ± 0.02	24.7[c]	24.9 ± 0.1[a]	0.75	0.77	– – –	– – –	$4d^{5}$	$4d^{4}5p$
W XXXV (W^{34+})	23.772 ± 0.02	24.121 ± 0.02	24[c, d]	24.2 ± 0.1[a]	0.82	0.87	– – –	– – –	$4d^{4}$	$4d^{3}5p$
W XXXVI (W^{35+})	23.178 ± 0.02	23.277 ± 0.02		23.300[c]	0.71	0.75	– – –	– – –	$4d^{3}$	$4d^{2}5p$
W XXXVII (W^{36+})	22.398 ± 0.01	22.543 ± 0.01	22.5 ± 0.1[a]	22.6[c]	0.68	0.71	– – –	– – –	$4d^{2}$	4d5p
	22.689 ± 0.01	22.787 ± 0.01	22.5 ± 0.1[a]		0.79	0.81	– – –	– – –	$4d^{2}$	4d5p
W XXXVIII (W^{37+})	21.156 ± 0.01	21.251 ± 0.01	20.9 ± 0.1[a, d]		0.68	0.71	– – –	– – –	$4p^{6}4d$	$4p^{6}5p$
	21.773 ± 0.01	21.821 ± 0.01	21.9[b]	22.0 ± 0.1[a]	0.83	0.93	– – –	– – –	$4p^{6}4d$	$4p^{6}5p$

[a] Data from [9].
[b] Data from [10].
[c] Data from [8].
[d] Data from [9].
[e] Data from [34].

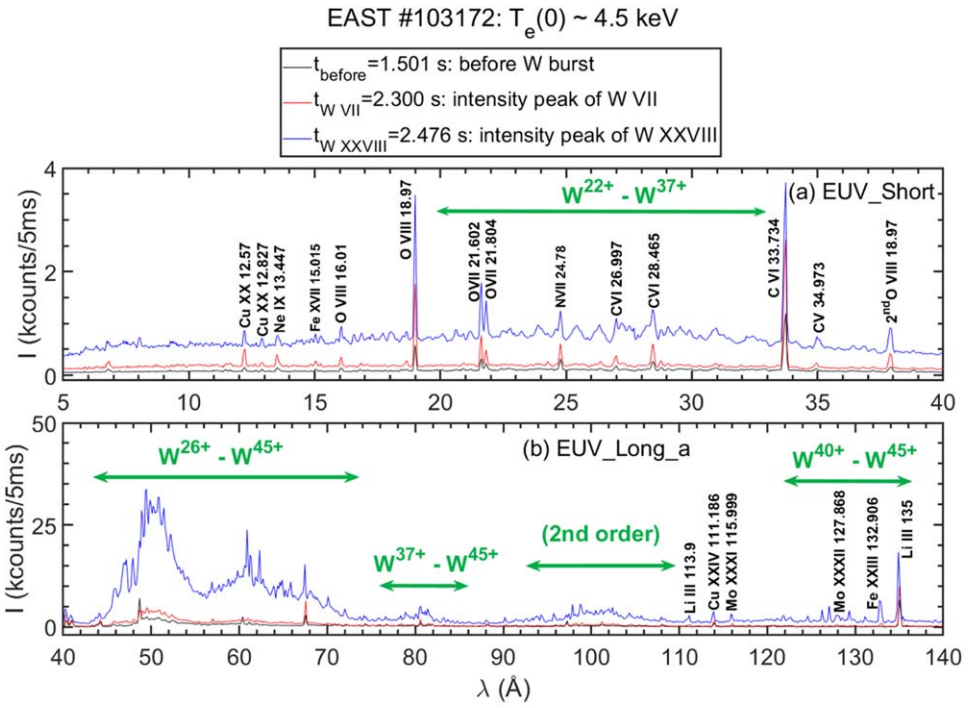

Figure 10. EUV spectra from high-electron temperature plasma (EAST #103172: $T_e(0) \sim 4.5$ keV) in wavelength ranges of (a) 5–40 Å (EUV_Short) and (b) 40–140 Å (EUV_Long_a) before (t = 1.501 s: black color) and during (t = 2.300 s: red color and 2.476 s: blue color) tungsten burst.

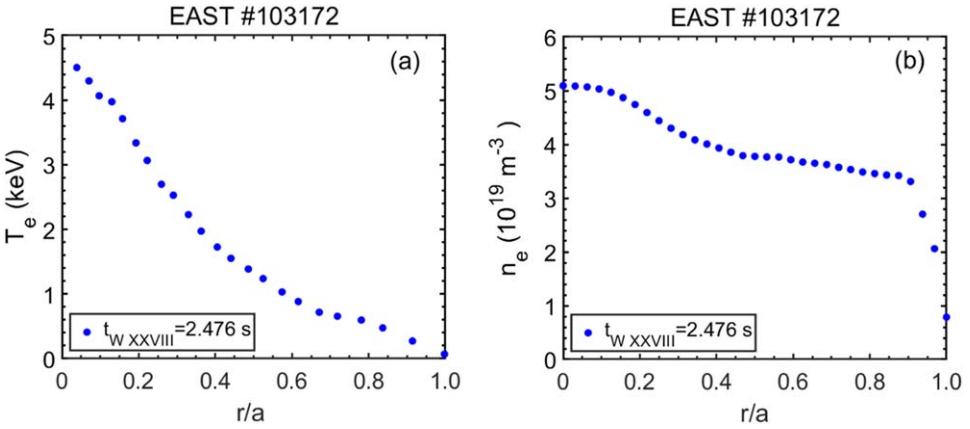

Figure 11. Radial profiles of (a) electron temperature measured by ECE and (b) electron density measured by POINT at t = 2.476 s in #103172 discharge. Horizontal axis means normalized minor radius (also see figure caption of figure 6).

high spectral resolution using CMOS detector ($\Delta\lambda_{1/2} = 0.092$ Å at 33.734 Å and $\Delta\lambda_{1/2} = 0.104$ Å at 115.999 Å) is also used to analyze the spectra in the wavelength range of 45–70 Å.

The tungsten spectra are observed using EUV_Short2_d spectrometer in FVB mode with long exposure time of 1 s/frame. The result is plotted in figure 12(a). The spectrum of figure 12(a) is created by adding two frames together during t = 2–4 s. Figure 12(b) shows a simple extension of figure 10(b) at t = 2.476 s, observed with EUV_Long_a spectrometer (grating: 1200 grooves/mm) using CCD detector ($\Delta\lambda_{1/2} = 0.183$ Å at 33.734 Å and $\Delta\lambda_{1/2} = 0.285$ Å at 115.999 Å). Comparing the spectrum between figures 12(a) and (b), one can see that the spectrum in figure 12(a) has better information on the tungsten spectral lines.

The tungsten UTA spectra in this wavelength range are mainly dominated by transitions among sublevels within n = 4 levels for tungsten ions below rhodium-like (W^{45+}) ionization stage. In the 45–48 Å wavelength range, the tungsten UTA spectra are mainly composed of 4d-4p transitions for WXXXVIII - WXLV (W^{37+} - W^{44+}). Shifting the wavelength to 48–60 Å range, the main transition changes to 4f-4d transitions for WXXVII - WXXXVIII (W^{26+} - W^{37+}). The transition finally changes to 4p-4s transitions for WXXVII - WXXXVIII (W^{26+} - W^{37+}) in the

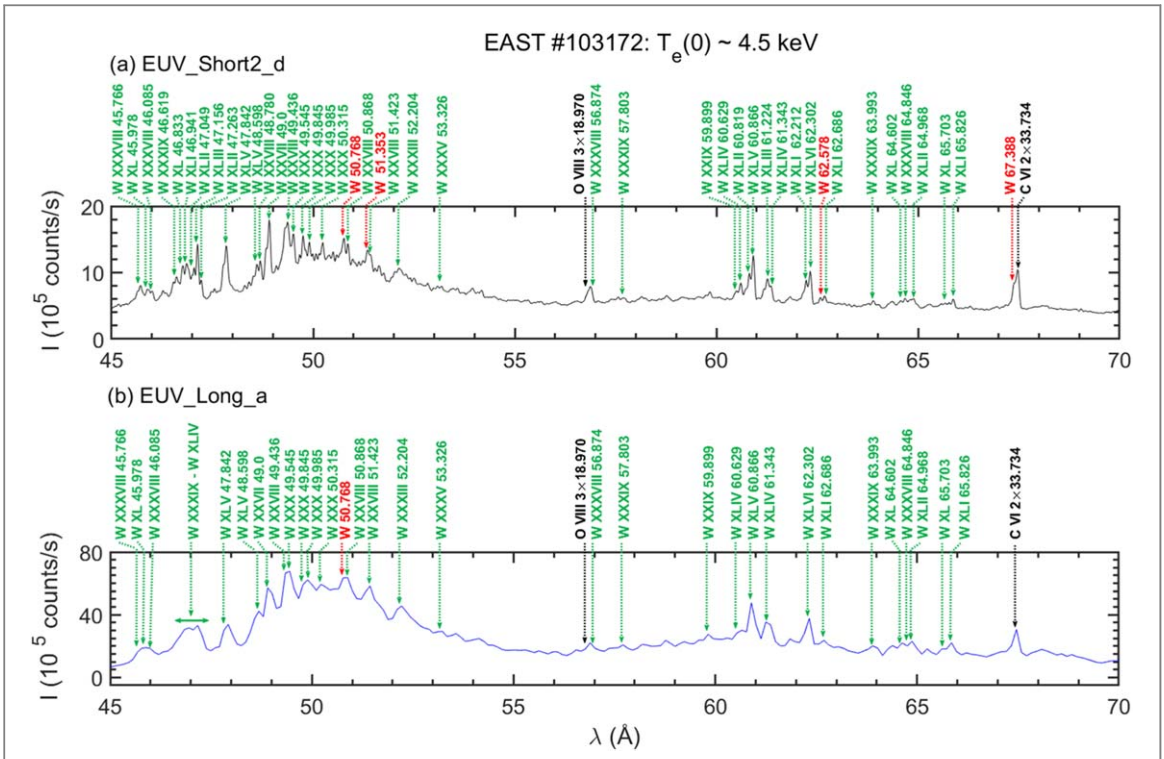

Figure 12. Enlarged tungsten spectra from high-electron temperature plasma (EAST #103172: $T_e(0) \sim 4.5$ keV) in wavelength range of 45–70 Å observed with (a) EUV_Short2_d (2400 grooves/mm, CMOS detector with 6.5×6.5 μm^2 pixel size, 2000 ms/frame) during t = 2–4 s and (b) EUV_Long_a (1200 grooves/mm, CCD detector with 26×26 μm^2 pixel size, 5 ms/frame) at t = 2.476 s during tungsten burst. Tungsten lines confirmed the ionization stage are indicated with green labels as W XXVII - W XLVI (W^{26+} - W^{45+}). Tungsten lines of which the ionization stage is unknown are denoted with red labels. Black labels indicate spectral lines from other impurity species.

tungsten UTA at the wavelength range of 48–60 Å. In addition, four tungsten lines are found in figure 12(a) (see red labels). Possible ionization stages of them are analyzed later in the discussion section.

Radial profiles of the tungsten UTA seen in figure 12 are examined for accurate line identification, since the vertical profile of impurity lines has been measured at the lower-half EAST plasma with EUV_Long2_d spectrometer (see blue LOS in figure 1). Some examples of the result are shown in figure 13 for the spectra in wavelength range of 45–70 Å observed at $t_{W\ XXVIII} = 2.476$ s. The bottom horizontal axis means vertical distance from the plasma center. The minus value indicates the distance below the midplane at Z = 0 (see figure 1). The top horizontal axis means the normalized minor radius. Then, the vertical distance of $-0.4\ \text{m} \leqslant Z \leqslant 0\ \text{m}$ corresponds to the normalized radial position of $0 \leqslant r/a \leqslant 0.62$. The radial profile of the tungsten spectra shown in figure 13 can accurately suggest the ionization stage of observed spectral lines from the peak position because the peak position changes against the ionization stage of tungsten ions based on the temperature profile shown in figure 11. For example, the peak position of WXXVII at 49.0 Å locates at r/a = 0.47 near the middle of plasma radius, while the peak position of WXLVI (W^{45+}) at 62.302 Å locates at r/a = 0.22 closer to plasma center. That is, the tungsten ion locates at certain electron temperature range near the ionization energy. Based on the radial profile measurement, we found that the tungsten line at 49.0 Å is W XXVII but not W XXIX (NIST database: 48.948 Å). The result is consistent with the observation in LHD [34]. The tungsten UTA at 45–70 Å is usually used for tungsten diagnostics in tokamak experiments, in particular, for evaluation of the tungsten concentration [49].

3.1.3. Tungsten UTA spectrum at 70–140 Å

Figure 14 shows tungsten spectra extended to 70–140 Å of figure 10(b). The 4d-4p transitions of WXXXVIII - WXLVI (W^{37+} - W^{45+}) appear in the wavelength range of 70–90 Å. The W XLVI at 72.086 Å is blended with Mo XXIV at 72.05 Å and the W XLIII at 83.262 Å is also blended with Cu XXII at 83.183 Å. These spectral structures can be easily resolved by analyzing temporal intensity behaviors of the tungsten lines. In the wavelength range of 90–120 Å, the tungsten lines are mainly occupied by the second-order spectra of tungsten UTA at 45–53 Å as denoted in figure 14. It is noted that the W XXVII at 2×49.0 Å and the W XXVIII at 2×49.436 Å are still observed with strong intensities. The second-order spectra of tungsten lines around 60–63 Å consisting of WXLI - WXLVI (W^{40+} - W^{45+}) are also appeared at 120–126 Å as denoted in figure 14(b). In the wavelength range of 120–140 Å four M1 forbidden transitions can be found, i.e. WXLIV (W^{43+}) at 126.325 Å ($3d^{10}4s^24p\ ^2P$,

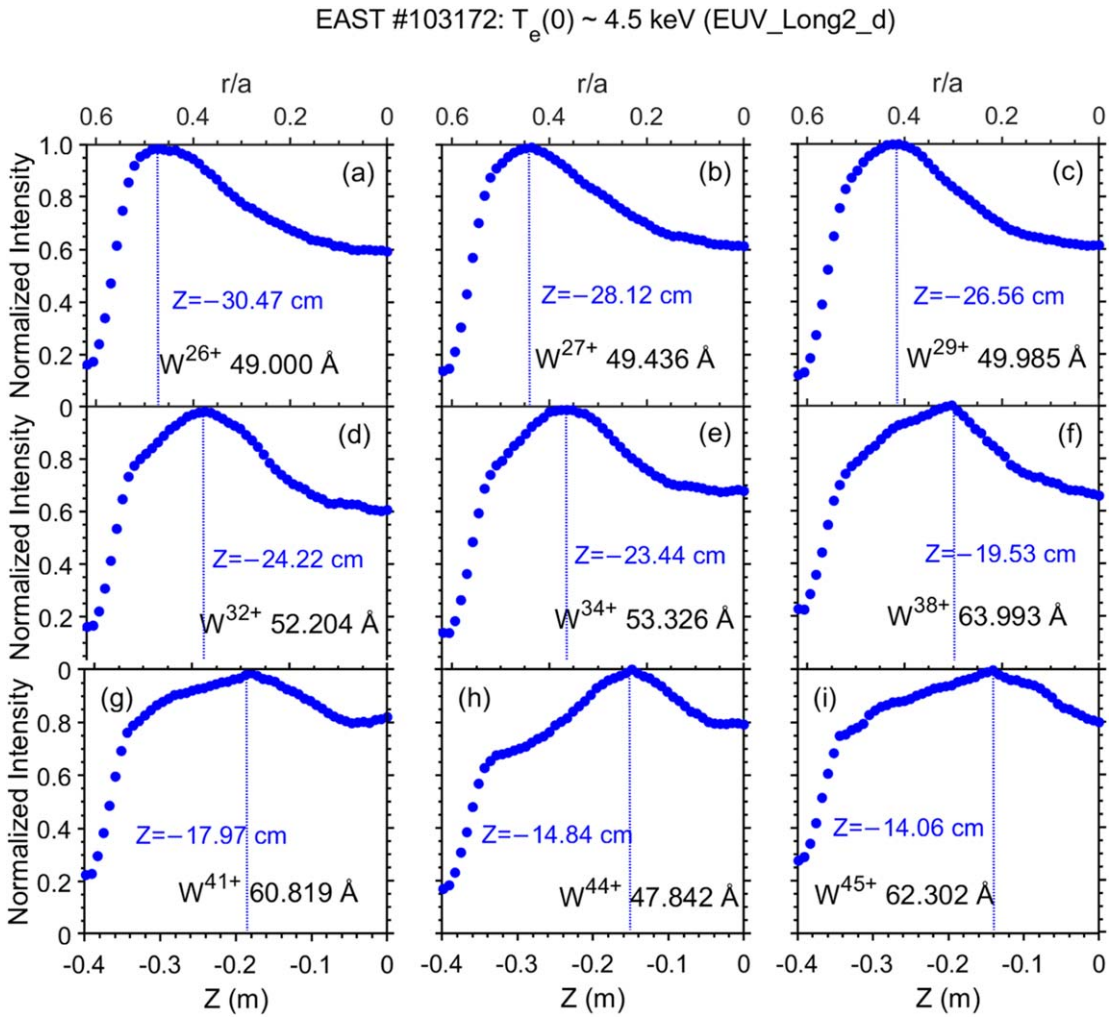

Figure 13. Vertical intensity profiles of tungsten lines in wavelength range of 45–65 Å (EAST #103172: $T_e(0) \sim 4.5$ keV, t = 2.476 s during tungsten burst) measured with EUV_Long2_d (20 ms/frame); (a) W^{26+}: 49.0 Å, (b) W^{27+}: 49.436 Å, (c) W^{29+}: 49.985 Å, (d) W^{32+}: 52.204 Å, (e) W^{34+}: 53.326 Å, (f) W^{38+}: 63.993 Å, (g) W^{41+}: 60.819 Å, (h) W^{44+}: 47.842 Å, and (i) W^{45+}: 62.302 Å. Horizontal axes at the bottom and top indicate plasma vertical position, Z, and normalized minor radius, r/a, respectively (see figures 1 and 6). The intensity is normalized at the peak position and the peak vertical position is denoted with vertical blue dotted lines.

J = 3/2→$3d^{10}4s^24p^2\ ^2P$, J = 1/2), WXLI (W^{40+}) at 128.598 Å ($3d^{10}4s^24p^4\ ^1D$, J = 2→$3d^{10}4s^24p^4\ ^3P$, J = 2), WXLII (W^{41+}) at 131.183 Å ($3d^{10}4s^24p^3\ ^2D$, J = 5/2→$3d^{10}4s^24p^4\ ^2D$, J = 3/2) and WXLIII (W^{42+}) at 135.491 Å ($3d^{10}4s^24p^2\ ^3P$, J = 1→$3d^{10}4s^24p^2\ ^3P$, J = 0). Electric quadrupole (E2) transition of WXLIII (W^{42+}) at 129.407 Å ($3d^{10}4s^24p^2\ ^1D$, J = 2→$3d^{10}4s^24p^2\ ^3P$, J = 0) can be found as an isolated line with strong intensity. In addition, three tungsten lines at 126.971 Å, 128.101 Å and 132.799 Å are identified as WXLVI (W^{45+}), WXLIV (W^{43+}) and WXLV (W^{44+}), respectively. Analyzing temporal behaviors of the tungsten line intensities and the vertical intensity profile, it is understood that the W XLIV line at 128.101 Å is blended with Mo XXXII at 127.868 Å and the W XLV at 132.799 Å is blended with Fe XXIII at 132.906 Å. The W XLIV at 126.325 Å and W XLIII at 129.407 Å have been used to evaluate the tungsten density in the core region of EAST and WEST plasmas [18, 50].

In the present identification mentioned above the reliability was also checked by measuring the radial profile of line intensities. Radial profile of the electron temperature and density measured at $t_{W\ XXVIII} = 3.876$ s in the #103162 discharge is plotted against the normalized plasma radius, as shown in figure 15. The central electron temperature reaches 6.2 keV. As an example of measured profile data, radial profiles of W XXVII (W^{26+}: 2 × 49.0 Å), WXXVIII (W^{27+}: 2 × 49.436 Å), WXXX (W^{29+}: 2 × 49.985 Å), W XLIII (W^{42+}: 129.407 Å), W XLIV (W^{43+}: 126.325 Å) and W XLVI (W^{45+}: 126.970 Å) are plotted in figure 16. From the figures, one can understand that the peak position of the radial profile shifts toward the plasma center with increase in the ionization stage of tungsten ions, e.g. r/a = 0.57 for W^{26+} and r/a = 0.24 for W^{45+}.

The tungsten lines identified at 15–140 Å in figures 12 and 14 are summarized in table 2 except for the unknown tungsten lines. Ionization stages of the tungsten lines (W XXVII - W XLVI: W^{26+} - W^{45+}), intensities and wavelengths from referred database and transitions are listed in the table with wavelengths and intensities

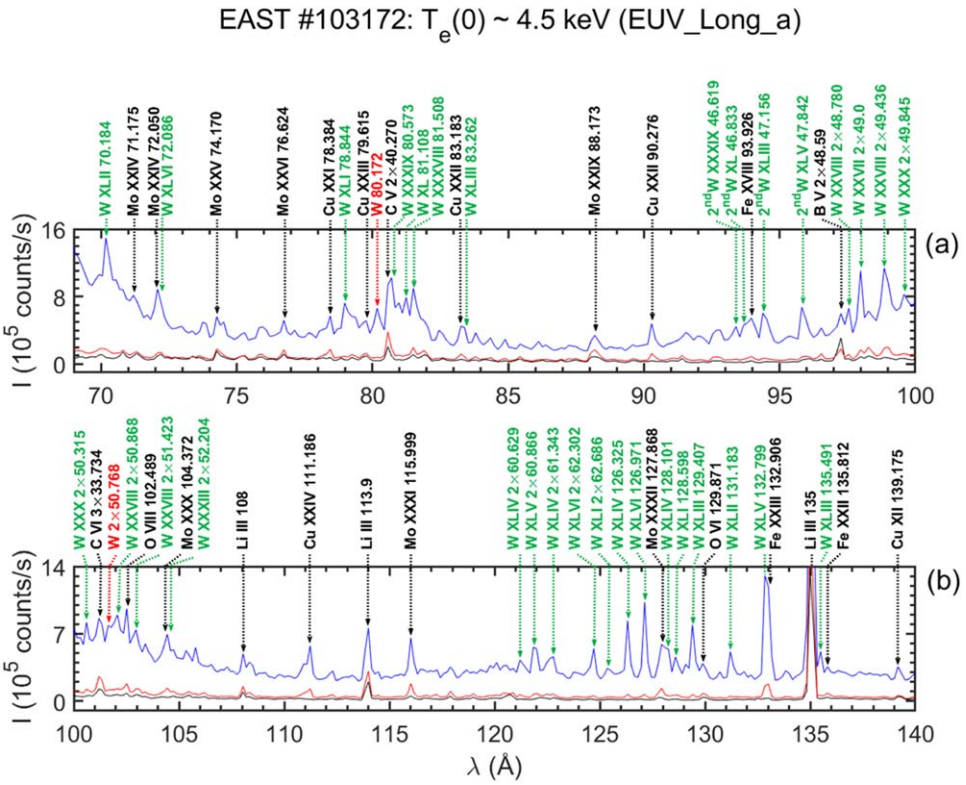

Figure 14. Enlarged tungsten spectra of figure 10(b) in wavelength range of 70–140 Å. Tungsten lines of W XXVII - W XLVI (W^{26+} - W^{45+}) identified here are denoted with green labels. Red and black labels indicate unknown tungsten lines and spectral lines from other impurity species intrinsically existing in EAST discharges, respectively.

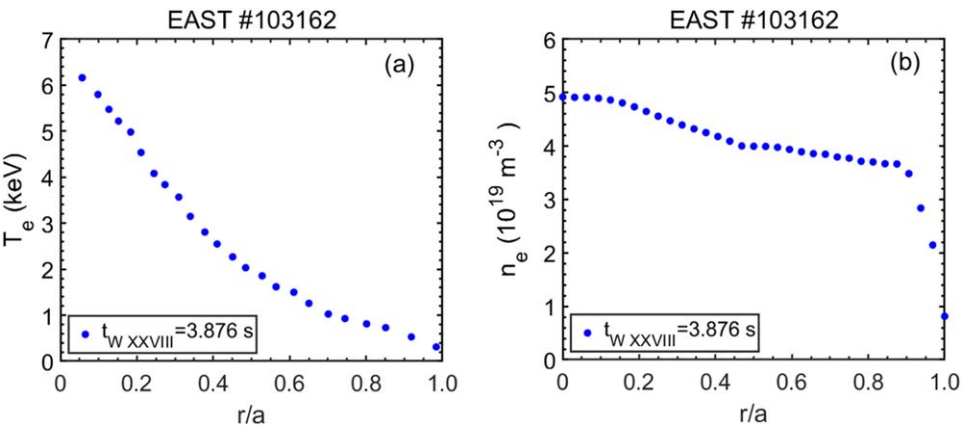

Figure 15. Radial profiles of (a) electron temperature measured by ECE and (b) electron density measured by POINT for t = 3.876 s during tungsten burst in #103162 discharge with higher electron temperature. Horizontal axis means normalized minor radius (also see figure caption of figure 6).

observed in the present work. Some transition data are not found in the reference data. Isolated tungsten lines without spectral merging are highlighted in bold in the table.

3.2. Identification of W V- W IX from low-ionized tungsten ions

3.2.1. Tungsten UTA spectrum at 140–330 Å

Figure 17 shows extended spectra of figure 7(c). In the wavelength range of 140–160 Å, third-order spectra of tungsten UTA with 4f-4d transitions are observed at 45–53 Å including W XXVIII (48.780 Å, 49.436 Å, 50.868 Å and 51.423 Å) and W XXX (49.845 Å and 50.315 Å), as shown in figure 17(a). Fourth-order spectra of these transitions are also seen in the 195–205 Å range (see figure 17(b)). The line identification of these higher-order tungsten UTA is also done based on the temporal behavior and radial profile analyses.

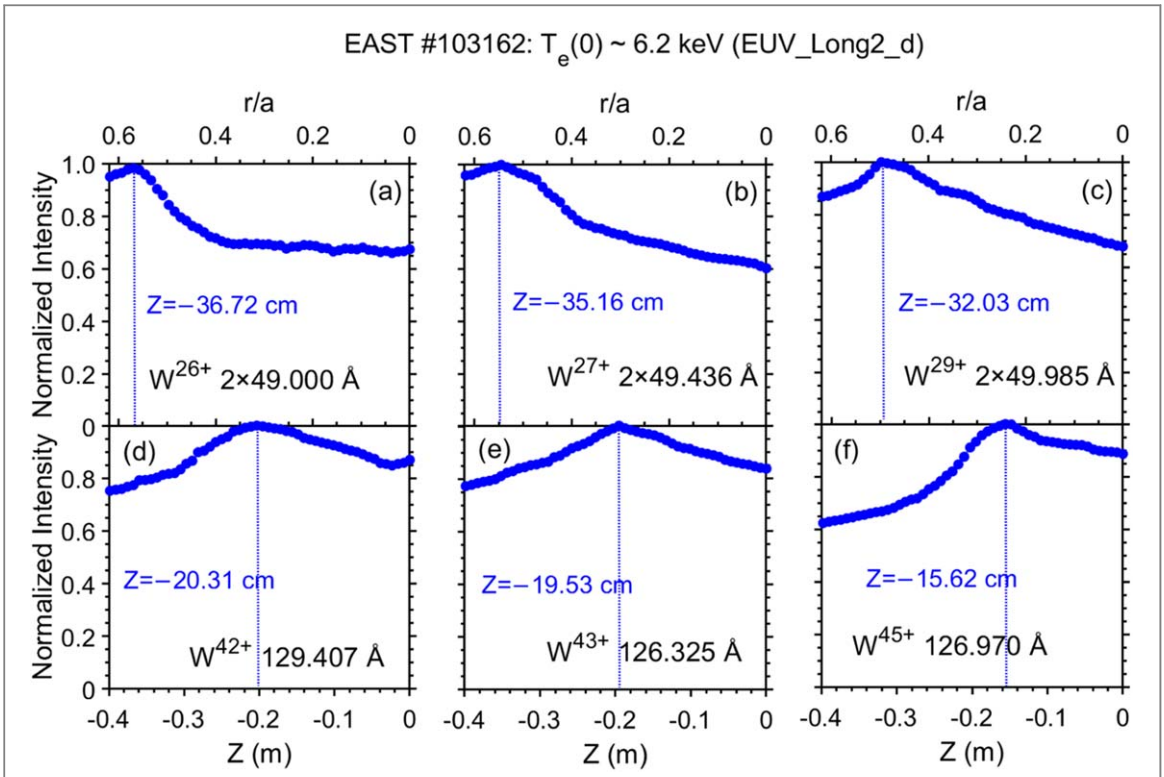

Figure 16. Vertical intensity profiles of tungsten lines in wavelength range of 95–130 Å (EAST #103162: $T_e(0) \sim 6.2$ keV, t = 3.876 s during tungsten burst); (a) W^{26+}: 2 × 49.000 Å, (b) W^{27+}: 2 × 49.436 Å, (c) W^{29+}: 2 × 49.985 Å, (d) W^{42+}: 129.407 Å, (e) W^{43+}: 126.325 Å and (f) W^{45+}: 126.970 Å. Horizontal axes at the bottom and top indicate plasma vertical position, Z, and normalized minor radius, r/a, respectively (see figures 1 and 6). The intensity is normalized at the peak position and the peak vertical position is denoted with vertical blue dotted lines.

Since experimental data of tungsten lines for W^{9+} - W^{26+} ions are very few in the wavelength range of 170–330 Å as reported in the previous study [45], the line identification is mainly carried out for W^{5+} - W^{8+} ions. Then, only W VI - W IX lines are identified in figure 17 with reference to previously published data from vacuum spark discharges by Ryabtsev *et al* [28], NIST [45] and magnetic-confinement fusion experiments (SSPX spheromak [7], LHD stellarator [13], JET tokamak [29] and HL-2A tokamak [14]). As shown in figures 17(a) and (b), ten W IX lines from W^{8+} ions are found in the wavelength range of 170–195 Å. Unfortunately, only one of ten W IX lines, 193.764 Å, is known as the transition with $4f^{13}5p^5\ ^3G$, J = 6→$4f^{13}5p^4 5d\ ^3H$, J = 6. The intensity of identified W IX lines is generally weak compared with W VII and W VIII lines described later. This result was consistent with the reference database [14, 28]. Then, the candidate for tungsten diagnostics seems to be only the W IX line at 194.725 Å because the intensity is not weak at all and the line is isolated from other impurity lines.

A large number of W VIII lines emitted from W^{7+} ions can be found in the wavelength range of 190–265 Å as seen in figures 17(b) and (c) [28]. Fifty-nine W VIII lines with 6s-5p, 5d-5p and 6d-5p transitions are identified by analyzing the wavelengths and intensities with reference to previously published data. The W VIII lines in the wavelength range of 197.5–202.0 Å with 6s-5p and 5d-5p transitions are observed with strong intensities as shown in figure 17(b), e.g. 198.781 Å, 199.947 Å, 200.530 Å and 201.700 Å. These lines may be useful for tungsten diagnostics. In the wavelength range of 225–255 Å in figure 17(c), the W VIII lines with 5d-5p transitions are seen with slightly stronger intensity, e.g. 238.285 Å, 252.253 Å, 252.896 Å and 253.540 Å. However, the intensity of those W VIII lines observed in this work at the two wavelength ranges is entirely different from results in the vacuum spark, whereas results in HL-2A and JET fusion devices show the same tendency as our results. The reason is probably in the different electron density range between the two types of devices. The W VIII lines in the wavelength ranges of 197.5–202.0 Å and 248–255 Å would be suitable for tungsten diagnostics in fusion devices.

Many W VII lines emitted from W^{6+} ions are seen in figures 17(a)–(d). A total of eleven W VII lines are found including two W VII lines with 6s-5p transitions (188.230 Å and 223.836 Å), six W VII lines with 5d-5p transitions (216.351 Å, 261.317 Å, 289.546 Å, 294.446 Å, 302.385 Å and 313.580 Å) and three W VII lines with 5f-5d transitions (321.142 Å, 324.654 Å and 326.802 Å). The intensities of W VII lines at 216.351 Å and 261.317 Å are very strong. As expected, the intensity observed here is consistent with results in other fusion devices like SSPX and HL-2A [7, 14]. The result also indicates density dependence of the W VII intensities as well as the result on the W VIII intensity. In any case, the two W VII lines at 216.351 Å and 261.317 Å can be an

Table 2. Isolated lines of W XXVII - W XLVI (W^{26+} - W^{45+}) from moderately and highly ionized tungsten ions identified in the present work. First column shows tungsten lines. Second column gives wavelengths, λ, determined in this work and taken from previously published data in the references. Third column gives intensities observed in this work and taken from previously published data. Label of '– – –' means the reference has no intensity information. Fourth column indicates lower and upper levels of the transition.

W^{q+}	λ (Å)		Intensities		Transitions	
	This work	Previous data	This work (10^{15} phs·m^{-2}·s^{-1}·Sr^{-1})	Previous data (a.u.)	Lower level	Upper level
W XXVII (W^{26+})	**49.000 ± 0.01**	**40.81–49.03**[a]	**4.69**	–	**$4d^{10}4f^2$**	**$4d^{10}4f5g$**
W XXVIII (W^{27+})	**48.780 ± 0.01**	**48.729**[b]	**5.06**	**15**	**$4d^{10}4f\,^2F^\circ_{7/2}$**	**$4d^9 4f(^1P^\circ)4\,f\,^2F_{7/2}$**
	49.436 ± 0.01	**49.403**[b]	**5.82**	**25**	**$4d^{10}4f\,^2F^\circ_{5/2}$**	**$4d^9 4f(^1P^\circ)4\,f\,^2D_{3/2}$**
	50.868 ± 0.01	**50.895**[b]	**5.55**	**15**	**$4d^{10}4f\,^2F^\circ_{7/2}$**	**$4d^9 4f(^1P^\circ)4\,f\,^2G_{9/2}$**
	51.423 ± 0.01	**51.457**[b]	**5.08**	**10**	**$4d^{10}4f\,^2F^\circ_{5/2}$**	**$4d^9 4f(^1P^\circ)4\,f\,^2G_{7/2}$**
W XXIX (W^{28+})	**59.799 ± 0.01**	**59.852**[b]	**2.41**	**1**	**$4d^{10}\,^1S_0$**	**$4d^9 4f\,^3D^\circ_1$**
W XXX (W^{29+})	**49.545 ± 0.01**	**49.5**[b]	**5.92**	–	**$4d^8 4p$**	**$4d^8 4d$**
	49.845 ± 0.01	**49.785**[b]	**5.17**	**30**	**$4d^9\,^2D_{5/2}$**	**$4d^8(^3F)4\,f\,^2F^\circ_{7/2}$**
	49.985 ± 0.01	49.938[b]	5.43	20	$4d^9\,^2D_{5/2}$	$4d^8(^1G)4\,f\,^2P^\circ_{3/2}$
	50.315 ± 0.01	50.265[b]	5.18	25	$4d^9\,^2D_{5/2}$	$4d^8(^3F)4\,f\,^2D^\circ_{5/2}$
W XXXIII (W^{32+})	52.204 ± 0.01	52.200[b]	3.97	–	unknown	unknown
W XXXV (W^{34+})	**53.326 ± 0.01**	**53.200**[b]	**2.56**	–	**unknown**	**unknown**
W XXXVIII (W^{37+})	**45.766 ± 0.01**	**45.781**[b]	**1.65**	**100**	**$4p^6 4d\,^2D_{3/2}$**	**$4p^5(^2P^\circ_{1/2})4d^2(^1D_2)\,(1/2,2)^\circ_{3/2}$**
	46.085 ± 0.01	46.064[b]	1.41	25	$4p^6 4d\,^2D_{5/2}$	$4p^5(^2P^\circ_{1/2})4d^2(^1G_4)\,(1/2,4)^\circ_{7/2}$
	56.874 ± 0.01	56.880[b]	1.92	35	$4p^6 4d\,^2D_{3/2}$	$4p^6 4f\,(0,5/2)^\circ_{5/2}$
	64.846 ± 0.01	**64.825**[b]	**2.04**	**16**	**$4p^6 4d\,^2D_{3/2}$**	**$4p^5(^2P^\circ_{3/2})4d^2(^3F_3)\,(3/2,3)^\circ_{3/2}$**
	81.508 ± 0.01	**81.457**[b]	**1.23**	**8**	**$4p^6 4d\,^2D_{3/2}$**	**$4p^5(^2P^\circ_{3/2})4d^2(^3F_2)\,(3/2,2)^\circ_{3/2}$**
W XXXIX (W^{38+})	46.619 ± 0.01	46.670[b]	2.35	100	$4p^6\,^1S_0$	$4p^5(^2P^\circ_{1/2})4d\,(1/2,3/2)^\circ_1$
	57.803 ± 0.01	57.717[b]	1.81	18	unknown	unknown
	63.993 ± 0.01	**63.883**[b]	**1.78**	**22**	**$4p^6\,^1S_0$**	**$4p^5(^2P^\circ_{3/2})4d\,(3/2,5/2)^\circ_1$**
	80.573 ± 0.01	80.640[b]	1.01	6	$4p^6\,^1S_0$	$4p^5(^2P^\circ_{3/2})4d\,(3/2,3/2)^\circ_1$
W XL (W^{39+})	45.978 ± 0.01	45.954[b]	1.68	1	unknown	unknown
	46.833 ± 0.01	46.827[b]	2.71	720	$4s^2 4p^5\,^2P^\circ_{3/2}$	$4s^2 4p^4(^1D_2)4d\,(2,3/2)_{1/2}$
	64.602 ± 0.01	**64.661**[b]	**1.95**	**200**	**$4s^2 4p^5\,^2P^\circ_{3/2}$**	**$4s^2 4p^4(^3P_2)4d\,(2,5/2)_{5/2}$**
	65.703 ± 0.01	**65.658**[b]	**1.61**	**80**	**$4s^2 4p^5\,^2P^\circ_{3/2}$**	**$4s^2 4p^4(^3P_2)4d\,(2,5/2)_{3/2}$**
	81.108 ± 0.01	81.153[b]	0.78	40	$4s^2 4p^5\,^2P^\circ_{3/2}$	$4s^2 4p^4(^3P_2)4d\,(2,3/2)_{5/2}$
W XLI (W^{40+})	**46.941 ± 0.01**	**46.957**[b]	**2.79**	**336**	**$4s^2 4p^4\,^3P_2$**	**$4s^2 4p^3(^2D^\circ_{5/2})4d\,(5/2,3/2)^\circ_3$**
	62.212 ± 0.01	62.193[b]	2.48	30	$4s^2 4p^4\,^1S_0$	$4s4p^5\,(1/2,3/2)^\circ_1$
	62.686 ± 0.01	**62.689**[b]	**2.09**	**74**	**$4s^2 4p^4\,^3P_2$**	**$4s4p^5\,(1/2,3/2)^\circ_2$**
	65.826 ± 0.01	**65.873**[b]	**1.97**	**100**	**$4s^2 4p^4\,^3P_2$**	**$4s^2 4p^3(^2P^\circ_{3/2})4d\,(3/2,5/2)^\circ_3$**
	78.844 ± 0.01	78.952[b]	0.71	32	unknown	unknown
	128.598 ± 0.01	**128.640**[b]	**0.84**	**220**	**$4\,s^2 4p^4\,^3P_2$**	**$4\,s^2 4p^4\,^1D_2$**

Table 2. (Continued.)

W^{q+}	λ (Å)		Intensities		Transitions	
	This work	Previous data	This work (10^{15} phs·m^{-2}·s^{-1}·Sr^{-1})	Previous data (a.u.)	Lower level	Upper level
W XLII (W^{41+})	47.049 ± 0.01	47.048[b]	2.73	73	$4s^24p^3\,^2D^\circ_{3/2}$	$4s^24p^2(^1D_2)4d\,(2,3/2)_{3/2}$
	47.263 ± 0.01	47.287[b]	2.92	100	$4s^24p^3\,^2D^\circ_{3/2}$	$4s^24p^2(^3P_1)4d\,(1,3/2)_{5/2}$
	60.819 ± 0.01	60.729[b]	2.54	23	$4s^24p^3\,^2D^\circ_{3/2}$	$4s(^2S_{1/2})4p^4\,(1/2,2)_{3/2}$
	64.968 ± 0.01	64.888[b]	2.06	18	$4s^24p^3\,^2D^\circ_{3/2}$	$4s(^2S_{1/2})4p^4(^3P_2)\,(1/2,2)_{5/2}$
	70.184 ± 0.01	**70.150** [h]	**1.36**	**8**	**$4\ s^24p^3\,^2D^\circ_{3/2}$**	**$4s^24p^2(^3P_0)4d\,(0,5/2)_{5/2}$**
	131.183 ± 0.01	**131.210**[b]	**0.78**	**20**	**$4s^24p^3\,^2D^\circ_{3/2}$**	**$4s^24p^3\,^2D^\circ_{3/2}$**
W XLIII (W^{42+})	47.156 ± 0.01	47.191[b]	2.92	100	$4s^24p^2\,^3P_0$	$4s^24p4d\,(1/2,3/2)^\circ_1$
	61.224 ± 0.01	**61.304**[b]	**3.10**	**55**	**$4s^24p^2\,^3P_0$**	**$4s(^2S_{1/2})4p^3(^2P^\circ_{3/2})(1/2,3/2)^\circ_1$**
	83.262 ± 0.01	83.289[b]	0.44	2	$4s^24p^2\,^1D_2$	$4s^24p4d\,(1/2,3/2)_2$
	129.407 ± 0.01	**129.41**[b]	**1.47**	**70**	**$4s^24p^2\,^3P_0$**	**$4s^24p^2\,^1D_2$**
	135.491 ± 0.01	**135.45**[b]	**1.04**	**40**	**$4s^24p^2\,^3P_0$**	**$4s^24p^2\,^3P_1$**
W XLIV (W^{43+})	**47.911 ± 0.01**	**47.903**[b]	**2.97**	**100**	**$4s^24p\,^2P^\circ_{1/2}$**	**$4s^24d\,^2D_{3/2}$**
	60.629 ± 0.01	60.616[b]	2.64	35	$4s^24p\,^2P^\circ_{1/2}$	$4s4p^2\,^2P_{1/2}$
	61.343 ± 0.01	**61.334**[b]	**3.10**	**62**	**$4s^24p\,^2P^\circ_{1/2}$**	**$4s4p^2\,^2D_{3/2}$**
	126.325 ± 0.01	**126.29**[b]	**1.48**	**80**	**$4s^24p\,^2P^\circ_{1/2}$**	**$4s^24p\,^2P^\circ_{3/2}$**
	128.101 ± 0.01	128.17[b]	0.98	50	$4\ s^24p\,^2P^\circ_{1/2}$	$4\ s4p^2\,^4P_{1/2}$
W XLV (W^{44+})	47.842 ± 0.01	47.9[b]	2.97	–	$4s4p\,(1/2,1/2)^\circ_1$	$4s4d\,(1/2,3/2)_1$
	48.598 ± 0.01	48.617[b]	3.71	9	$4s4p\,(1/2,1/2)^\circ_1$	$4s4d\,(1/2,3/2)_2$
	60.493 ± 0.01	60.581[b]	2.49	–	$4s4p\,(1/2,1/2)^\circ_0$	$4p^2\,(1/2,3/2)_1$
	60.866 ± 0.01	**60.930**[b]	**4.18**	**100**	**$4s^2\,^1S_0$**	**$4s4p\,(1/2,3/2)^\circ_1$**
	132.799 ± 0.01	132.88[b]	2.23	100	$4s^2\,^1S_0$	$4s4p\,(1/2,1/2)^\circ_1$
W XLVI (W^{45+})	**62.302 ± 0.01**	**62.336**[b]	**3.32**	**100**	**$4s\,^2S_{1/2}$**	**$4p\,^2P^\circ_{3/2}$**
	72.086 ± 0.01	71.976[b]	0.82	70	$4p\,^2P_{3/2}$	$4d\,^2D_{5/2}$
	126.971 ± 0.01	**126.998**[b]	**1.84**	**20**	**$4s\,^2S_{1/2}$**	**$4p\,^2P^\circ_{1/2}$**

Useful lines for tungsten diagnostics are highlighted in bold.

[a] Data from [33].

[b] Data from NIST database [45].

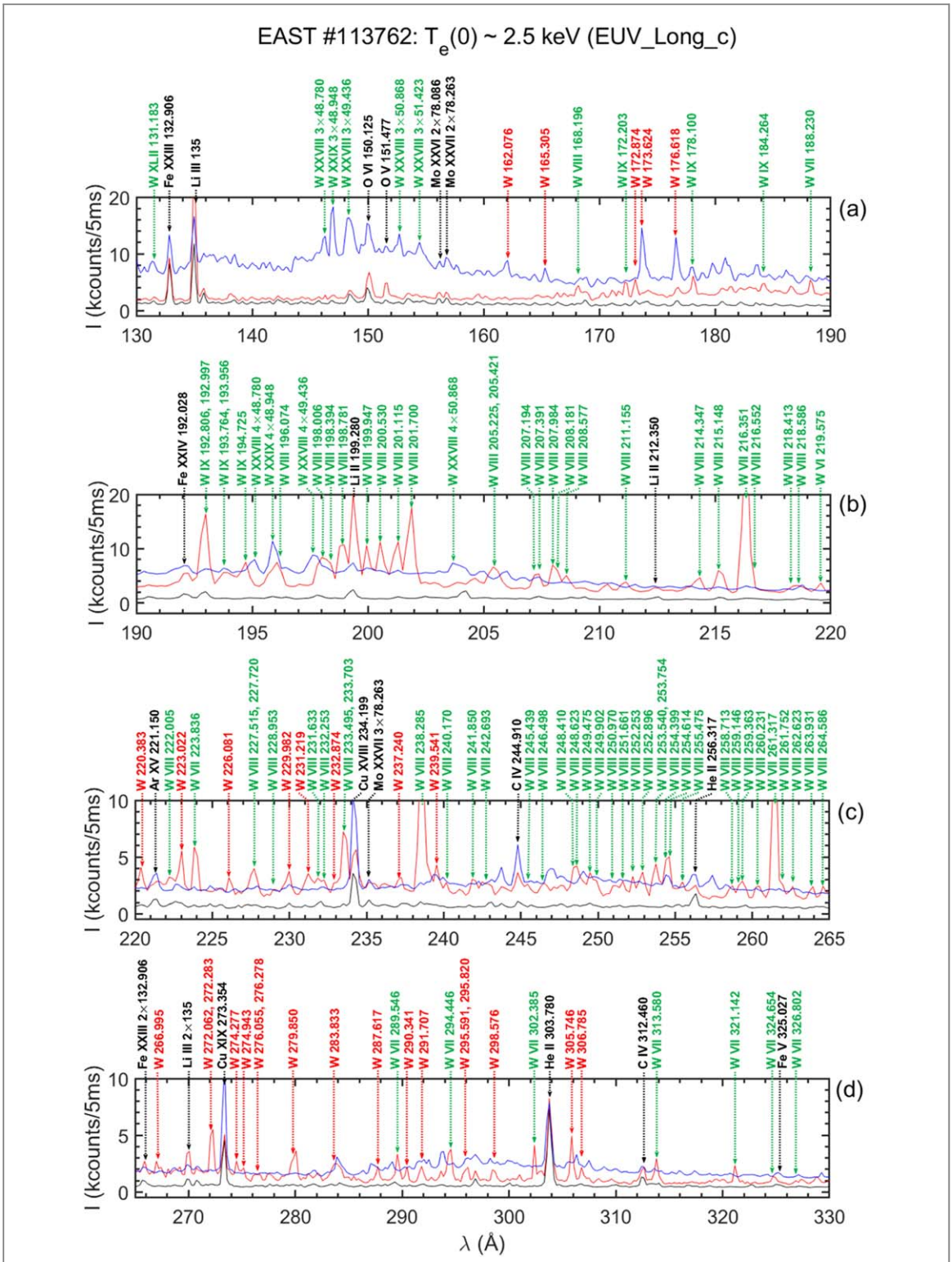

Figure 17. Tungsten spectra in wavelength ranges of (a) 130–190 Å, (b) 190–220 Å, (c) 220–265 Å and (d) 265–330 Å. Tungsten lines analyzed here are composed of W VI - W XLII (W^{5+} - W^{41+}) indicated with green labels. Red and black labels indicate unknown tungsten lines and spectral lines from other impurity species intrinsically existing in EAST discharges. The spectra are observed at three discharge timings as shown in figure 5.

extremely good tool for tungsten diagnostics in the SOL and/or divertor regions of fusion plasmas. In HL-2A tokamak, the tungsten influx rate was evaluated using the WVII line for the first time [14].

One W VI line emitted from W^{5+} ions is observed at 219.575 Å (see figure 17(b)). The intensity is very weak. The same line is also found in SSPX spheromak [7]. Through this study we could not find any tungsten lines from ionization stages lower than W^{5+} ions.

The ionization stage of these tungsten lines is also checked by analyzing the temporal behavior similar to previous results mentioned before. Although there is no significant difference in the temporal behavior among

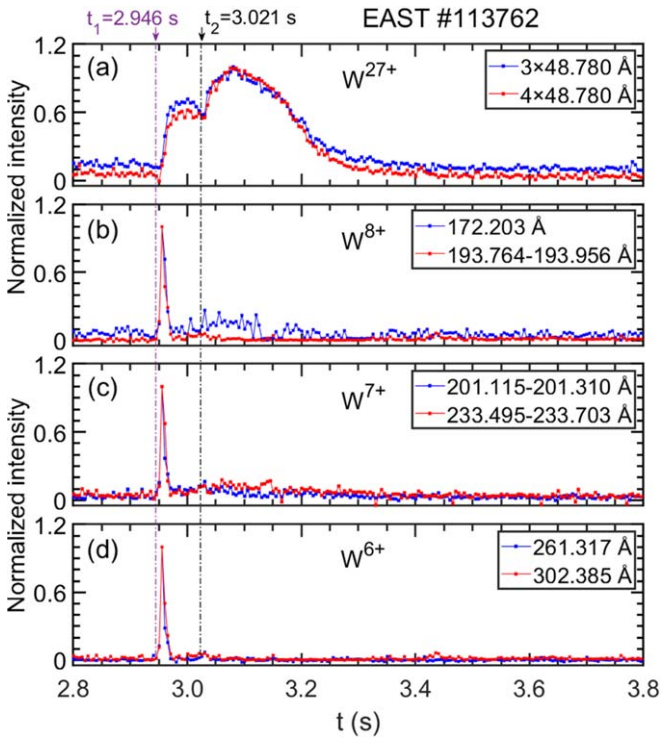

Figure 18. Time behaviors of tungsten line intensities for (a) W^{27+}: 48.780 Å (3rd and 4th orders), (b) W^{8+}: 172.203 Å and 193.764–193.956 Å, (c) W^{7+}: 201.115–201.310 Å and 233.495–233.703 Å and (d) W^{6+}: 261.317 Å and 302.385 Å. Vertical dash-dotted lines at t = 2.946 s and 3.021 s indicate start and end of first W burst, respectively.

W^{6+} - W^{8+} ions due to very close ionization energies of E_i = 65–160 eV, a noticeable difference in the temporal behavior can be seen for moderately ionized tungsten ions, as shown in figure 18. The line emission from low-ionized tungsten ions of W^{6+} - W^{8+} quickly increases the intensity and meet the maximum intensity at t = 2.956 s just after the tungsten burst. As the tungsten ions after the tungsten burst are transferred from the plasma edge region to the plasma core region, the W^{6+} - W^{8+} ions entirely disappear at t = 2.970 s. In contrast, the line emission from W^{27+} ions increases the intensity after disappearance of the line emission from W^{6+} - W^{8+} ions and keeps a sufficient intensity level for a long time until t = 3.021 s (see figure 18(a)). The spectral appearance of W XXVIII over a long time period suggests a long confinement time of tungsten ions in the core region of tokamak plasmas.

The tungsten W V - W IX lines at 160–330 Å analyzed here are summarized in table 3. In the table 3, first column shows the tungsten ionization stages, and second and third columns give the wavelength from this work and referred database, respectively. The line intensity observed in this work and referred database is listed in fourth and fifth columns, respectively. Lower and upper levels of the transition are shown in sixth column. Some tungsten lines have no transitions due to a lack of database. The tungsten lines which seem to be useful for diagnostics are highlighted in bold in the table.

In figure 17 several tungsten lines are indicated with red labels. These lines were carefully examined by analyzing the temporal behavior after the tungsten burst in many EAST discharges and finally determined to be the spectral line arising from tungsten ions. However, it was difficult to determine the ionization stage of such tungsten lines indicated in red color due to a lack of information on the lines in the database and previous publications. Based on the temporal behavior, four moderately ionized tungsten lines are found in the wavelength range of 160–180 Å, i.e. 162.076 Å, 165.305 Å, 173.624 Å and 176.618 Å. Those are estimated to be tungsten lines arising from W^{27+} - W^{37+} ions. Using the same method, most of tungsten lines seen in the wavelength range of 220–480 Å are determined to belong to low-ionized tungsten ions of W^{4+} - W^{8+}. Some tungsten lines are isolated from other lines showing relatively high intensities, e.g. 223.022 Å, 272.062 Å and 305.746 Å. The tungsten lines indicated in red color in figure 17 are summarized in table 4 as an unknown tungsten line. The wavelengths determined in this work are shown in first column, and the ionization stages estimated through this work and the observed intensities are listed in second and third columns, respectively.

3.2.2. Tungsten spectrum at 330–480 Å

The EUV spectra are also observed in the wavelength range of 270–480 Å as shown in figure 7(d). However, no tungsten line was found in the spectrum. The reason probably originates in the radial position in the line-of-

Table 3. Isolated lines of W V - W IX (W^{4+} - W^{8+}) from low-ionized tungsten ions identified in the present work. First column shows tungsten lines. Second column gives wavelengths, λ, determined in this work and taken from previously published data in the references. Third column gives intensities observed in this work and taken from previously published data. Label of '———' means the reference has no intensity information. Fourth column indicates lower and upper levels of transition.

W^{q+}	λ (Å)		Intensities		Transitions	
	This work	Previous data	This work (10^{15} phs·m^{-2}·s^{-1}·Sr^{-1})	Previous data (a.u.)	Lower level	Upper level
W IX (W^{8+})	172.203 ± 0.05	172.038[a]	1.56	309	unknown	unknown
	178.100 ± 0.03	178.115[a]	1.83	97		
		178.140[a]		95		
	184.264 ± 0.02	184.200[a]	1.49	248		
		184.271[a]		117		
	192.806 ± 0.01	192.834[a]	4.10	541		
	192.997 ± 0.01	193.091[a]	4.71	132		
	193.764 ± 0.01	**193.830**[a]	**1.85**	**696**	**$4f^{13}5p^5\,{}^3G_6$**	**$4f^{13}5p^4(^3P)5d\,{}^3H_6$**
	193.956 ± 0.01	193.999[a]	1.83	362	unknown	unknown
	194.725 ± 0.01	194.646[a]	2.25	1000		
W VIII (W^{7+})	168.196 ± 0.05	168.381[a]	1.29	300	$4f^{13}5p^6\,{}^1F_{5/2}$	$4f^{13}5p^5 6s\ 7/2$
	196.074 ± 0.01	196.093[a]	2.51	640	$4f^{13}5p^6\,{}^2F_{5/2}$	$4f^{13}5p^5 6s\ 7/2$
	198.006 ± 0.01	197.835[a]	2.53	720	$4f^{13}5p^6\,{}^2F_{5/2}$	$4f^{12}5p^6 5d\ 3/2$
		197.941[a]		410	$4f^{13}5p^6\,{}^2F_{5/2}$	$4f^{12}5p^6 5d\ 5/2$
	198.394 ± 0.01	198.171[a]	2.51	590	$4f^{13}5p^6\,{}^2F_{7/2}$	$4f^{13}5p^5 6s\ 9/2$
		198.229[a]		670	$4f^{13}5p^6\,{}^2F_{5/2}$	$4f^{13}5p^5 6s\ 5/2$
	198.781 ± 0.01	**198.779**[a]	**3.60**	**740**	**$4f^{13}5p^6\,{}^2F_{7/2}$**	**$4f^{13}5p^5 6s\ 7/2$**
	199.947 ± 0.01	**199.875**[a]	**3.68**	**710**	**$4f^{13}5p^6\,{}^2F_{7/2}$**	**$4f^{13}5p^5 6s\ 5/2$**
	200.530 ± 0.01	**200.367**[a]	**3.92**	**710**	**$4f^{13}5p^6\,{}^2F_{5/2}$**	**$4f^{13}5p^5 5d\ 5/2$**
		200.483[a]		**730**	**$4f^{13}5p^6\,{}^2F_{7/2}$**	**$4f^{13}5p^5 5d\ 7/2$**
	201.115 ± 0.01	**201.079**[a]	**3.08**	**440**	**$4f^{13}5p^6\,{}^2F_{5/2}$**	**$4f^{13}5p^5 6s\ 5/2$**
	201.310 ± 0.01	**201.205**[a]	**3.96**	**700**	**$4f^{13}5p^6\,{}^2F_{5/2}$**	**$4f^{13}5p^5 6s\ 7/2$**
	201.700 ± 0.01	**201.739**[a]	**4.16**	**770**	**$4f^{13}5p^6\,{}^2F_{7/2}$**	**$4f^{13}5p^5 5d\ 9/2$**
	201.895 ± 0.01	**201.864**[a]	**6.23**	**710**	**$4f^{13}5p^6\,{}^2F_{5/2}$**	**$4f^{13}5p^5 5d\ 7/2$**
	205.225 ± 0.02	205.221[a]	1.98	620	$4f^{13}5p^6\,{}^2F_{5/2}$	$4f^{12}5p^6 5d\ 3/2$
	205.421 ± 0.02	205.479[a]	2.45	660	$4f^{14}5p^5\,{}^2P_{3/2}$	$4f^{14}5p^4 6\ s\ 3/2$
	207.194 ± 0.02	207.092[a]	1.93	270	$4f^{14}5p^5\,{}^2P_{1/2}$	$4f^{14}5p^4 6s\ 1/2$
	207.391 ± 0.02	207.466[a]	2.02	340	$4f^{14}5p^5\,{}^2P_{3/2}$	$4f^{13}5p^5 6d\ 3/2$
	207.984 ± 0.03	207.884[a]	2.65	260	$4f^{13}5p^6\,{}^2F_{7/2}$	$4f^{14}5p^4 5d\ 5/2$
	208.181 ± 0.03	208.227[a]	2.31	170	$4f^{14}5p^5\,{}^2P_{3/2}$	$4f^{14}5p^4 6\ s\ 5/2$
	208.577 ± 0.03	208.420[a]	1.95	660	$4f^{14}5p^5\,{}^2P_{3/2}$	$4f^{14}5p^4 5d\ 5/2$
		208.543[a]		490	$4f^{14}5p^5\,{}^2P_{1/2}$	$4f^{14}5p^4 6s\ 3/2$

Table 3. (Continued.)

W^{q+}	λ (Å)		Intensities		Transitions	
	This work	Previous data	This work (10^{15} phs·m^{-2}·s^{-1}·Sr^{-1})	Previous data (a.u.)	Lower level	Upper level
	211.155 ± 0.04	211.027[a]	1.54	670	$4f^{14}5p^{5}\,^{2}P_{3/2}$	$4f^{14}5p^{4}5d\ 3/2$
	214.347 ± 0.04	214.229[a]	1.71	690	$4f^{14}5p^{5}\,^{2}P_{3/2}$	$4f^{12}5p^{6}5d\ 5/2$
	215.148 ± 0.05	215.055[a]	2.37	600	$4f^{14}5p^{5}\,^{2}P_{3/2}$	$4f^{12}5p^{6}5d\ 5/2$
	216.552 ± 0.05	216.596[a]	3.83	460	$4f^{14}5p^{5}\,^{2}P_{3/2}$	$4f^{12}5p^{6}5d\ 3/2$
	218.413 ± 0.05	218.429[a]	1.49	550	$4f^{14}5p^{5}\,^{2}P_{3/2}$	$4f^{12}5p^{6}5d\ 3/2$
	218.586 ± 0.05	218.507[a]	1.51	400	$4f^{14}5p^{5}\,^{2}P_{3/2}$	$4f^{12}5p^{6}5d\ 3/2$
	222.005 ± 0.06	221.909[a]	1.50	220	$4f^{13}5p^{6}\,^{2}F_{5/2}$	$4f^{12}5p^{6}5d\ 5/2$
	227.515 ± 0.05	227.497[a]	1.75	340	$4f^{13}5p^{6}\,^{2}F_{7/2}$	$4f^{12}5p^{6}5d\ 7/2$
	227.720 ± 0.05	227.617[a]	2.02	440	$4f^{14}5p^{5}\,^{2}P_{1/2}$	$4f^{14}5p^{4}5d\ 1/2$
	228.953 ± 0.05	229.011[a]	1.10	410	$4f^{13}5p^{6}\,^{2}F_{5/2}$	$4f^{12}5p^{6}5d\ 7/2$
	231.633 ± 0.04	231.629[a]	1.62	510	$4f^{14}5p^{5}\,^{2}P_{3/2}$	$4f^{12}5p^{6}5d\ 5/2$
	232.253 ± 0.04	232.176[a]	1.53	460	$4f^{13}5p^{6}\,^{2}F_{7/2}$	$4f^{12}5p^{6}5d\ 7/2$
	233.495 ± 0.04	233.525[a]	2.72	190	$4f^{13}5p^{6}\,^{2}F_{7/2}$	$4f^{12}5p^{6}5d\ 7/2$
	233.703 ± 0.04	233.709[a]	2.36	550	$4f^{13}5p^{6}\,^{2}F_{5/2}$	$4f^{12}5p^{6}5d\ 5/2$
	238.285 ± 0.02	238.243[a]	2.92	310	$4f^{13}5p^{6}\,^{2}F_{5/2}$	$4f^{12}5p^{6}5d\ 5/2$
	240.170 ± 0.01	240.107[a]	1.44	810	$4f^{13}5p^{6}\,^{2}F_{7/2}$	$4f^{12}5p^{6}5d\ 9/2$
	241.850 ± 0.01	241.867[a]	1.6	960	$4f^{13}5p^{6}\,^{2}F_{7/2}$	$4f^{12}5p^{6}5d\ 9/2$
	242.693 ± 0.01	242.819[a]	1.4	420	$4f^{13}5p^{6}\,^{2}F_{7/2}$	$4f^{12}5p^{6}5d\ 7/2$
	245.439 ± 0.02	245.474[a]	1.38	470	$4f^{13}5p^{6}\,^{2}F_{5/2}$	$4f^{12}5p^{6}5d\ 5/2$
	246.498 ± 0.02	246.362[a]	1.44	780	$4f^{13}5p^{6}\,^{2}F_{7/2}$	$4f^{12}5p^{6}5d\ 9/2$
	248.410 ± 0.02	248.508[a]	2.18	490	$4f^{13}5p^{6}\,^{2}F_{5/2}$	$4f^{12}5p^{6}5d\ 5/2$
	248.623 ± 0.02	248.649[a]	2.24	690	$4f^{13}5p^{6}\,^{2}F_{5/2}$	$4f^{12}5p^{6}5d\ 7/2$
	249.475 ± 0.03	249.533[a]	1.94	960	$4f^{14}5p^{5}\,^{2}P_{3/2}$	$4f^{14}5p^{4}5d\ 5/2$
	249.902 ± 0.03	249.873[a]	1.56	820	$4f^{13}5p^{6}\,^{2}F_{7/2}$	$4f^{12}5p^{6}5d\ 9/2$
	250.970 ± 0.03	250.978[a]	1.32	420	$4f^{13}5p^{6}\,^{2}F_{5/2}$	$4f^{12}5p^{6}5d\ 5/2$
	251.661 ± 0.03	251.584[a]	1.53	790	$4f^{13}5p^{6}\,^{2}F_{5/2}$	$4f^{12}5p^{6}5d\ 7/2$
	252.253 ± 0.04	252.203[a]	1.76	960	$4f^{13}5p^{6}\,^{2}F_{7/2}$	$4f^{13}5p^{5}5d\ 7/2$
	252.896 ± 0.03	252.740[a]	1.98	930	$4f^{14}5p^{5}\,^{2}P_{3/2}$	$4f^{13}5p^{5}5d\ 3/2$
		252.862[a]		790	$4f^{13}5p^{6}\,^{2}F_{7/2}$	$4f^{13}5p^{5}5d\ 7/2$
	253.540 ± 0.04	253.541[a]	1.73	820	$4f^{13}5p^{6}\,^{2}F_{5/2}$	$4f^{12}5p^{6}5d\ 5/2$
	253.754 ± 0.04	253.812[a]	2.37	1000	$4f^{13}5p^{6}\,^{2}F_{7/2}$	$4f^{12}5p^{6}5d\ 7/2$
	254.399 ± 0.04	254.294[a]	2.57	930	$4f^{13}5p^{6}\,^{2}F_{5/2}$	$4f^{12}5p^{6}5d\ 7/2$
	254.614 ± 0.04	254.551[a]	2.72	1000	$4f^{13}5p^{6}\,^{2}F_{5/2}$	$4f^{12}5p^{6}5d\ 3/2$
	255.475 ± 0.04	255.401[a]	1.53	860	$4f^{13}5p^{6}\,^{2}F_{7/2}$	$4f^{13}5p^{5}5d\ 9/2$

Table 3. (Continued.)

W^{q+}	λ (Å)		Intensities		Transitions	
	This work	Previous data	This work (10^{15} phs·m^{-2}·s^{-1}·Sr^{-1})	Previous data (a.u.)	Lower level	Upper level
	258.713 ± 0.04	258.592[a]	1.35	980	$4f^{13}5p^6\,^2F_{7/2}$	$4f^{13}5p^5 5d\ 5/2$
	259.146 ± 0.04	259.069[a]	1.39	280	$4f^{14}5p^5\,^2P_{1/2}$	$4f^{14}5p^4 5d\ 3/2$
	259.363 ± 0.04	259.419[a]	1.57	920	$4f^{14}5p^5\,^2P_{3/2}$	$4f^{13}5p^5 5d\ 5/2$
	260.231 ± 0.04	260.146[a]	1.28	290	$4f^{13}5p^6\,^2F_{7/2}$	$4f^{13}5p^5 5d\ 9/2$
	261.752 ± 0.03	261.767[a]	1.63	680	$4f^{13}5p^6\,^2F_{7/2}$	$4f^{13}5p^5 5d\ 7/2$
	262.623 ± 0.03	262.637[a]	1.33	530	$4f^{13}5p^6\,^2F_{7/2}$	$4f^{13}5p^5 5d\ 9/2$
	263.931 ± 0.03	263.787[a]	1.32	300	$4f^{13}5p^6\,^2F_{5/2}$	$4f^{13}5p^5 5d\ 7/2$
	264.586 ± 0.02	264.644[a]	1.34	320	$4f^{13}5p^6\,^2F_{5/2}$	$4f^{13}5p^5 5d\ 5/2$
W VII (W^{6+})	**188.230 ± 0.01**	**188.159**[b]	**1.72**	**800**	**$4f^{14}5p^6\,^1S_0$**	**$4f^{14}5p^5(^2P°_{1/2})6s\ (1/2,1/2)°_1$**
	216.351 ± 0.03	**216.219**[b]	**14.85**	**500**	**$4f^{14}5p^6\,^1S_0$**	**$4f^{14}5p^5(^2P°_{1/2})5d\ (1/2,3/2)°_1$**
	223.836 ± 0.06	**223.846**[b]	**2.88**	**300**	**$4f^{14}5p^6\,^1S_0$**	**$4f^{14}5p^5(^2P°_{3/2})6s\ (3/2,1/2)°_1$**
	261.317 ± 0.03	**261.387**[b]	**7.61**	**3000**	**$4f^{14}5p^6\,^1S_0$**	**$4f^{14}5p^5(^2P°_{3/2})5d\ (3/2,5/2)°_1$**
	289.546 ± 0.04	289.526[b]	1.93	300	$4f^{14}5p^6\,^1S_0$	$4f^{13}(^2F°_{5/2})5p^6 5d\ (5/2,5/2)°_1$
	294.446 ± 0.02	294.376[b]	2.20	200	$4f^{14}5p^6\,^1S_0$	$4f^{13}(^2F°_{5/2})5p^6 5d\ (5/2,3/2)°_1$
	302.385 ± 0.03	302.272[b]	2.44	700	$4f^{14}5p^6\,^1S_0$	$4f^{13}(^2F°_{7/2})5p^6 5d\ (7/2,5/2)°_1$
	313.580 ± 0.04	313.573[b]	1.79	30	$4f^{14}5p^6\,^1S_0$	$4f^{14}5p^5(^2P°_{3/2})5d\ (3/2,3/2)°_1$
	321.142 ± 0.06	321.211[b]	1.43	150	$4f^{13}(^2F°_{5/2})5p^6 5d\ (5/2,3/2)°_4$	$4f^{13}(^2F°_{5/2})5p^6 5\ f(5/2,5/2)_4$
	324.654 ± 0.08	324.563[b]	1.24	500	$4f^{13}(^2F°_{7/2})5p^6 5d\ (7/2,3/2)°_4$	$4f^{13}(^2F°_{7/2})5p^6 5\ f(7/2,5/2)_6$
	326.802 ± 0.08	326.644[b]	1.13	500	$4f^{13}(^2F°_{7/2})5p^6 5d\ (7/2,3/2)°_4$	$4f^{13}(^2F°_{7/2})5p^6 5\ f(7/2,5/2)_5$
	332.855 ± 0.07	332.842[b]	0.28	500	$4f^{13}(^2F°_{7/2})5p^6 5d\ (7/2,5/2)°_4$	$4f^{13}(^2F°_{7/2})5p^6 5f\ (7/2,7/2)_5$
	333.536 ± 0.07	333.509[b]	5.36	200	$4f^{13}(^2F°_{7/2})5p^6 5d\ (7/2,5/2)°_4$	$4f^{13}(^2F°_{7/2})5p^6 5f\ (7/2,7/2)_4$
	334.251 ± 0.07	334.311[b]	5.29	500	$4f^{13}(^2F°_{5/2})5p^6 5d\ (5/2,5/2)°_5$	$4f^{13}(^2F°_{5/2})5p^6 5f\ (5/2,7/2)_6$
	337.119 ± 0.07	337.045[b]	4.95	450	$4f^{13}(^2F°_{7/2})5p^6 5d\ (7/2,5/2)°_3$	$4f^{13}(^2F°_{7/2})5p^6 5f\ (7/2,7/2)_4$
	338.823 ± 0.07	338.679[b]	6.64	500	$4f^{13}5p^6 5d\ (7/2,5/2)°_5$	$4f^{13}(^2F°_{7/2})5p^6 5f\ (7/2,7/2)_6$
W VI (W^{5+})	219.575 ± 0.05	219.461[c]	1.65	–––	5p	5d
	382.133 ± 0.02	**382.145**[b]	**18.09**	**20**	**$5d\,^2D_{3/2}$**	**$5f\,^2F°_{5/2}$**
	394.072 ± 0.06	**394.133**[b]	**20.41**	**20**	**$5d\,^2D_{5/2}$**	**$5f\,^2F°_{7/2}$**
W V (W^{4+})	**434.327 ± 0.06**	**434.439**[b]	**11.14**	**10**	**$5d^2\,^3P_2$**	**$5d(^2D_{3/2})7p\ (3/2,1/2)°_1$**
	449.673 ± 0.06	449.649[b]	8.41	70	$5d^2\,^3P_1$	$5d(^2D_{5/2})5f(5/2,5/2)°_2$

Useful lines for tungsten diagnostics are highlighted in bold.

[a] Data from [28].

[b] Data from [45].

[c] Data from [23].

Table 4. Isolated tungsten lines newly confirmed in long wavelength range of 70–480 Å. First column gives wavelengths, λ, determined in this work. Ionization stages estimated from temporal behavior and radial intensity profile are listed in the second column. Third column shows observed intensity. At present transitions are 'unknown' as indicated in the last column.

λ (Å)	Ionization stages	Intensities (10^{15} phs·m^{-2}·s^{-1}·Sr^{-1})	Transitions
80.172 ± 0.01	W^{38+} - W^{45+}	0.67	
162.076 ± 0.05	W^{26+} - W^{37+}	2.51	unknown
165.305 ± 0.05	W^{26+} - W^{37+}	2.15	
172.874 ± 0.05	W^{26+} - W^{37+}	1.02	
173.624 ± 0.05	W^{26+} - W^{37+}	4.30	
176.618 ± 0.04	W^{26+} - W^{37+}	3.85	
220.383 ± 0.05	W^{4+} - W^{8+}	1.85	
223.022 ± 0.06	W^{4+} - W^{8+}	2.68	
226.081 ± 0.05	W^{4+} - W^{8+}	1.48	
229.982 ± 0.05	W^{4+} - W^{8+}	1.82	
231.219 ± 0.04	W^{4+} - W^{8+}	1.77	
232.874 ± 0.04	W^{4+} - W^{8+}	1.40	
237.240 ± 0.02	W^{4+} - W^{8+}	1.68	
239.541 ± 0.01	W^{4+} - W^{8+}	2.26	
266.995 ± 0.02	W^{4+} - W^{8+}	1.51	
272.062 ± 0.01	W^{4+} - W^{8+}	2.78	
272.283 ± 0.01	W^{4+} - W^{8+}	2.81	
274.227 ± 0.02	W^{4+} - W^{8+}	1.55	
274.943 ± 0.02	W^{4+} - W^{8+}	1.21	
276.055 ± 0.03	W^{4+} - W^{8+}	0.84	
276.278 ± 0.03	W^{4+} - W^{8+}	0.88	
279.850 ± 0.04	W^{4+} - W^{8+}	2.08	
283.833 ± 0.05	W^{4+} - W^{8+}	1.79	
287.617 ± 0.05	W^{4+} - W^{8+}	1.31	
290.341 ± 0.04	W^{4+} - W^{8+}	1.30	
291.707 ± 0.04	W^{4+} - W^{8+}	1.32	
295.591 ± 0.02	W^{4+} - W^{8+}	0.95	
295.820 ± 0.02	W^{4+} - W^{8+}	1.14	
298.576 ± 0.01	W^{4+} - W^{8+}	1.16	
305.746 ± 0.05	W^{4+} - W^{8+}	2.95	
306.785 ± 0.05	W^{4+} - W^{8+}	1.32	

sight of the EUV_Long_b spectrometer. Since the ionization stage from which the tungsten line is emitted becomes low in longer wavelength range such as figures 7(c) and (d), a line-of-sight of the spectrometer observing the plasma edge with lower electron temperature is optimal for measuring line emissions from low-ionized tungsten ions. The line-of-sight of the EUV_Long_b is closer to the core compared to that of the EUV_Long_c with which the tungsten line from low-ionized tungsten ions could be observed as shown in figure 7(c) (see also figure 1). In order to analyze the line emission from low-ionized tungsten ions in the wavelength range of 330–480 Å, therefore, the study was continued for discharges with lower electron temperatures.

A typical result from low-temperature EAST discharges is shown in figure 19 (EAST #113757: $T_e(0) \sim$ 1.0 keV). Three discharge timings are chosen as in the previous figures, i.e. before tungsten burst (t_{before} = 7.626 s: black lines), during tungsten burst ($t_{W\ VII}$ =7.716 s: red lines) and after tungsten burst ($t_{W\ XXVIII}$ =7.781 s: blue lines). Radial profile of the electron temperature and density measured at $t_{W\ VII}$ = 7.716 s in the #113757 discharge is plotted against the normalized plasma radius, as shown in figure 20. Figures 19(a) and (b) are observed with the EUV_Long_c and EUV_Long_b in the wavelength ranges of 130–330 Å and 270–480 Å, respectively, as well as figures 7(c) and (d). Several emission lines from low-ionized tungsten ions are observed in the wavelength range of 180–330 Å as shown in figure 19(a). These tungsten spectra identified in figure 19(a) are basically consistent with the result in figure 17.

Figure 21 shows expanded spectra of figure 19(b). Many emission lines from low-ionized tungsten ions can be found in the spectra. Results of the line identification in the wavelength range of 270–330 Å are shown in figure 21(a). All tungsten lines clearly identified in this wavelength range arise from W VII (see green labels in figure 21(a)). The tungsten lines denoted with red labels could not be found the ionization stage and transition. Results of these lines are added to the tables 3 and 4.

The line identification of tungsten spectra is also done in the wavelength range of 330–480 Å, as shown in figure 21(b). Five W VII spectra with 5f-5d transitions are found with weak intensities at 332.855 Å, 333.536 Å, 334.251 Å, 337.119 Å and 338.823 Å. We found two W VI spectral lines with 5f-5d transitions at 382.133 Å and

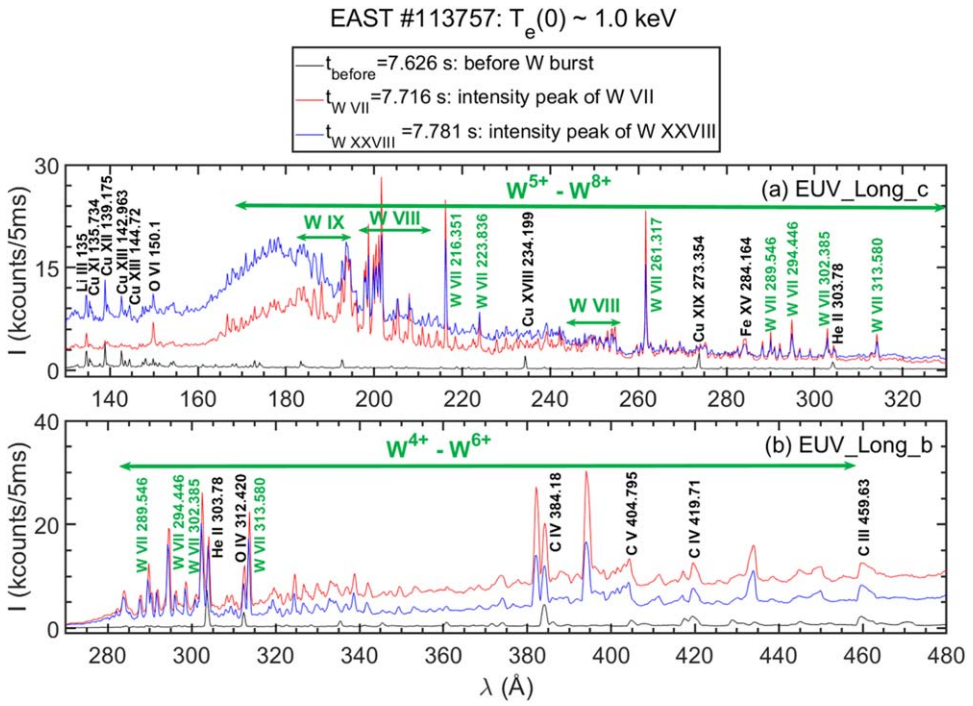

Figure 19. Tungsten spectra from lower electron temperature plasma (EAST #113757: $T_e(0) \sim 1.0$ keV) in wavelength range of 130–480 Å; (a) 130–330 Å (EUV_Long_c) and (b) 270–480 Å (EUV_Long_b). Three spectra are taken before ($t_{before} = 7.626$ s: black color) and after ($t_{W\ VII} = 7.716$ s: red color and $t_{W\ XXVIII} = 7.781$ s: blue color) tungsten burst, similar to that shown in previous figures.

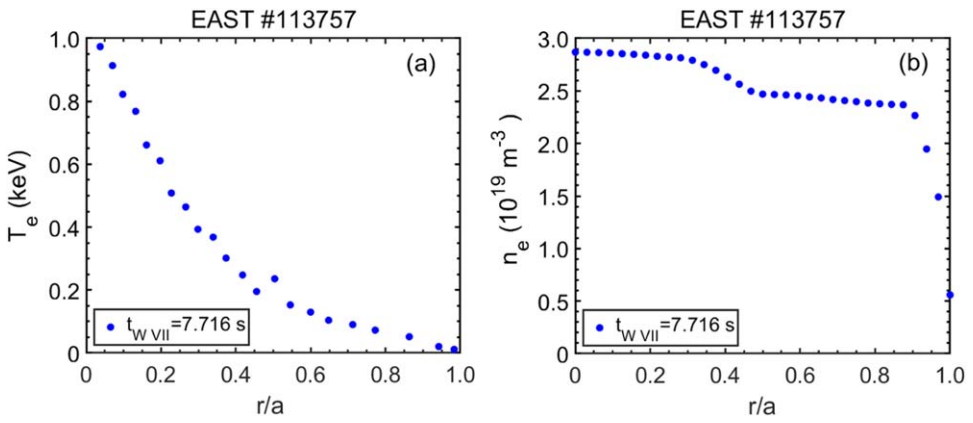

Figure 20. Radial profiles of (a) electron temperature measured by ECE and (b) electron density measured by POINT for t = 7.716 s during tungsten burst in #113757 discharge with lower electron temperature. Horizontal axis means normalized minor radius (also see figure caption of figure 6).

394.072 Å are emitted with relatively strong intensities. The intensity observed here is considerably higher than that in the database, as shown in table 3. These two W VI lines may be also used for tungsten diagnostics in the divertor plasma with extremely low electron temperature because the W^{5+} ion stays in the electron temperature range between 51.6 eV and 64.77 eV in corona equilibrium. It is noted here that the electron temperature in the vicinity of separatrix X-point is typically below 100 eV in on-going tokamak devices, although it largely depends on the magnetic field connection length from the divertor. In addition, two weak W V spectra with 5 f - 5d transitions are observed at 434.327 Å and 449.673 Å in figure 21(b). Information on these W VII and W V lines is also added to the table 3.

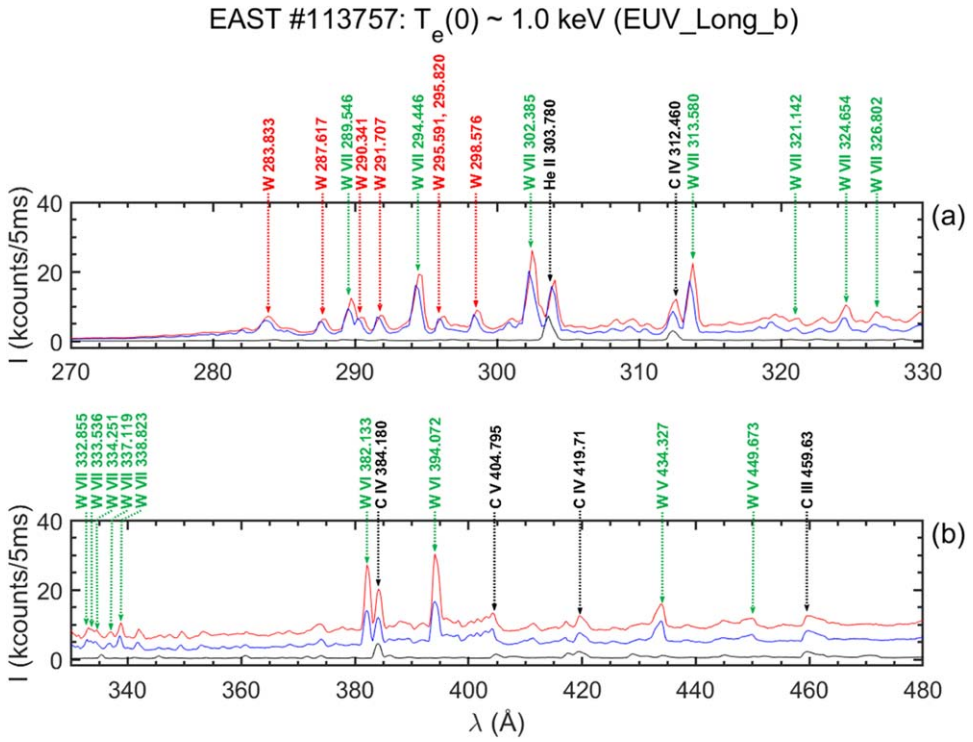

Figure 21. Enlarged tungsten spectra of figure 19(b) in wavelength ranges of (a) 270–330 Å and (b) 330–480 Å. Tungsten lines analyzed here are composed of W V - W VII (W^{4+} - W^{6+}) denoted with green labels. Red and black labels indicate unknown tungsten lines and spectral lines from other impurity species intrinsically existing in EAST discharges. Meaning of three spectra with different colors is the same as figure 19.

4. Discussions

4.1. Analysis of tungsten UTA spectra at 50–70 Å using radial profile measurement

In figure 12, we only showed results of the line identification on strong and isolated tungsten lines based on the existing database. However, the analysis of the UTA spectra was not entirely straightforward. The analysis of temporal behavior alone was insufficient to determine the ionization stage. Then, the analysis of the radial profile was attempted to understand the tungsten UTA spectra in the wavelength range of 50–70 Å. Figure 22 shows extended spectra of figure 12. Fifteen narrow wavelength intervals are chosen as indicated with areas filled in red, since those intervals include small tungsten peak, e.g. 52.03–52.334 Å and 67.811–68.195 Å. In addition to the narrow wavelength intervals, four peak positions are also chosen for the analysis (see figure 12). Results of the radial profile measurement on the tungsten UTA spectra are shown in figure 23. One can understand that the radial profile obtained here is remarkably similar to that on the isolated tungsten line shown in figure 13.

The peak position of the radial profiles shown in figure 23 was analyzed in the same way as in figure 13. It is noted here that both figures 13 and 23 are obtained from the same discharge of #103172. Therefore, the ionization stage at the wavelength interval or the spectral peak in figure 23 can be easily determined by referring to the result obtained in figure 13, if the radial profile has a clear peak position. That is, tungsten spectra with peak positions of $Z = -26.56$ cm at 50.768 Å (figure 23(a)), $Z = -25.0$ cm at 51.353 Å (figure 23(b)), $Z = -28.12$ cm at 59.064–59.292 Å (figure 23(f)) and $Z = -24.22$ cm at 67.388 Å (figure 23(i)) are determined to arise from W^{29+}, W^{31+}, W^{27+} and W^{32+}, respectively. It is interesting that the wavelength interval of 59.064–59.292 Å can be explained by only a single ionization stage of W^{27+} (W XXVIII).

The method mentioned above can be also applied for the radial profile with flatter peak. The flat peak shape suggests that several spectral lines arising from tungsten ions in adjacent ionization stages are emitted in the narrow wavelength interval. Therefore, the ionization stages of tungsten ions existing in the flat peak can be also inferred from the relationship between the peak position and tungsten ionization stage which has been already examined in figure 13. For example, the peak position of the radial profile in figure 23(c) can be estimated to range in $-25.0\ \text{cm} \leqslant Z \leqslant -19.53$ cm. Then, we understand this range corresponds to the peak position of W^{31+} - W^{38+} ions. The same analysis is done for other flat profile cases. Results on the examined ionization stages are indicated in each figure of figure 23.

Results of the analysis on the UTA spectra are summarized in table 5. First column shows wavelengths observed in this work, and second and third columns give the range of ionization stages evaluated from the

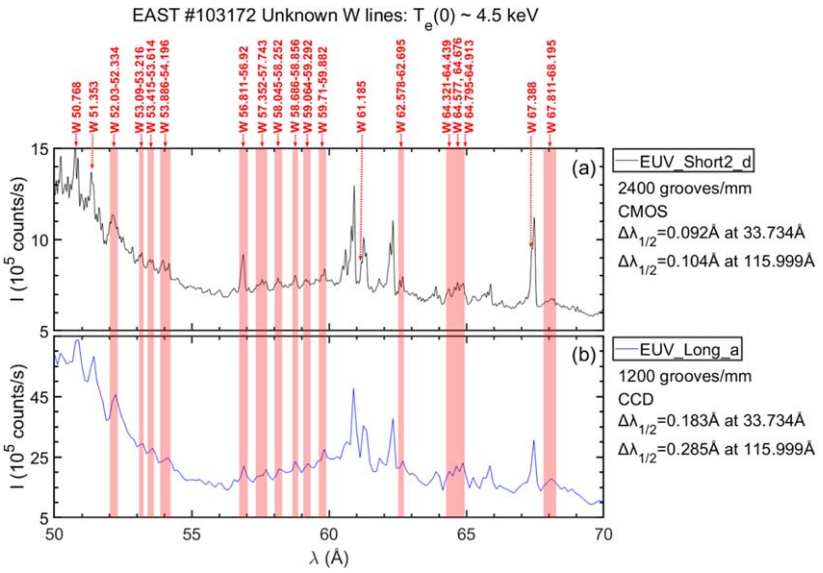

Figure 22. Tungsten spectra in wavelength range of 50–70 Å measured with (a) EUV_Short2_d and (b) EUV_Long_a. Data of figure 22 are the same as figure 12. Red shaded areas indicate wavelength interval of unknown tungsten lines for examination of the ionization stage by analyzing the radial profile.

vertical profile and the intensity of observed tungsten lines or wavelength intervals, respectively. The transition is unknown for all spectra.

4.2. Effect of electron temperature on the tungsten UTA spectra at 140–220 Å

Two tungsten spectra at 130–330 Å observed in EAST discharges with different central electron temperatures of $T_e(0) = 2.5$ and 1.0 keV are shown in figures 7(c) and 19(a), respectively. One can notice from the spectra that the UTA spectrum appears at the wavelength range of 140–220 Å in figure 19(a) taken from the low-temperature plasma ($T_e(0) = 1.0$ keV), while such the UTA spectrum almost disappears in figure 7(c) taken from the high-temperature plasma ($T_e(0) = 2.5$ keV). Although 3rd-order light of the UTA spectrum at 45–70 Å still remains at 135–210 Å in figure 7(c), it entirely disappears from the spectra in figure 19(a) because tungsten ions of W^{26+} - W^{45+} consisting of the UTA spectrum at 45–70 Å do not exist in such low-temperature plasmas.

When the UTA spectrum at 140–220 Å in figure 19(a) is carefully examined, we notice the peak position of the UTA spectrum changes from 185 Å to 197 Å between $t_{W\ VII} = 7.716$ s and $t_{W\ XXVIII} = 7.781$ s. As the central electron temperature continuously decreases after the tungsten burst as shown in figure 5, the electron temperature at $t_{W\ XXVIII} = 7.781$ s is lower than that at $t_{W\ VII} = 7.716$ s. Then, it indicates that the peak position of the UTA shifts toward shorter wavelength side when the electron temperature decreases. In EBIT experiments, on the other hand, the UTA spectrum at 140–220 Å can be studied by changing the beam energy. The peak position of the UTA was located near 200 Å when the beam energy was 70–135 eV [23]. When the beam energy increased to 400 eV, the peak position shifted to 175 Å. Increasing the beam energy above 400 eV, the UTA spectrum finally disappeared. This EBIT experiment can well explain the present result.

The UTA spectrum at 140–220 Å is composed of W^{5+} - W^{8+} ions as shown in figure 19(a). A little change in the electron temperature during the tungsten burst modifies the charge distribution of tungsten ions among W^{5+} - W^{8+} consisting of the UTA spectrum, and resultantly the peak position is changed as a function of discharge time after the tungsten burst. However, once the electron temperature is sufficiently high such as seen in figure 7, the low-ionized tungsten ions of W^{5+} - W^{8+} are pushed to the plasma peripheral region and moderately ionized tungsten ions are dominant in high-temperature plasmas. As a consequence, the intensity of line emissions from low-ionized tungsten ions are very weak, and line emissions arising from W^{26+} - W^{37+} ions appear in the wavelength range of 140–220 Å as seen in figure 17(a), i.e. 173.624 Å and 176.618 Å from W^{26+} - W^{37+} ions (see also table 4). Similar results are also seen for the UTA spectrum at 10–50 Å observed in LHD experiments [11]. The UTA spectrum largely changes the peak position when the central electron temperature decreases from 1.7 keV to 0.13 keV. The peak shift is also accompanied by a change in the combination of dominant transitions consisting of the UTA spectrum, i.e. 5f-4d and 5p-4d at $T_e(0) \sim 1.5$ keV, 6g-4f and 5g-4f at $T_e(0) \sim 0.6$ keV and 5g-4f at $T_e(0) \sim 0.13$ keV.

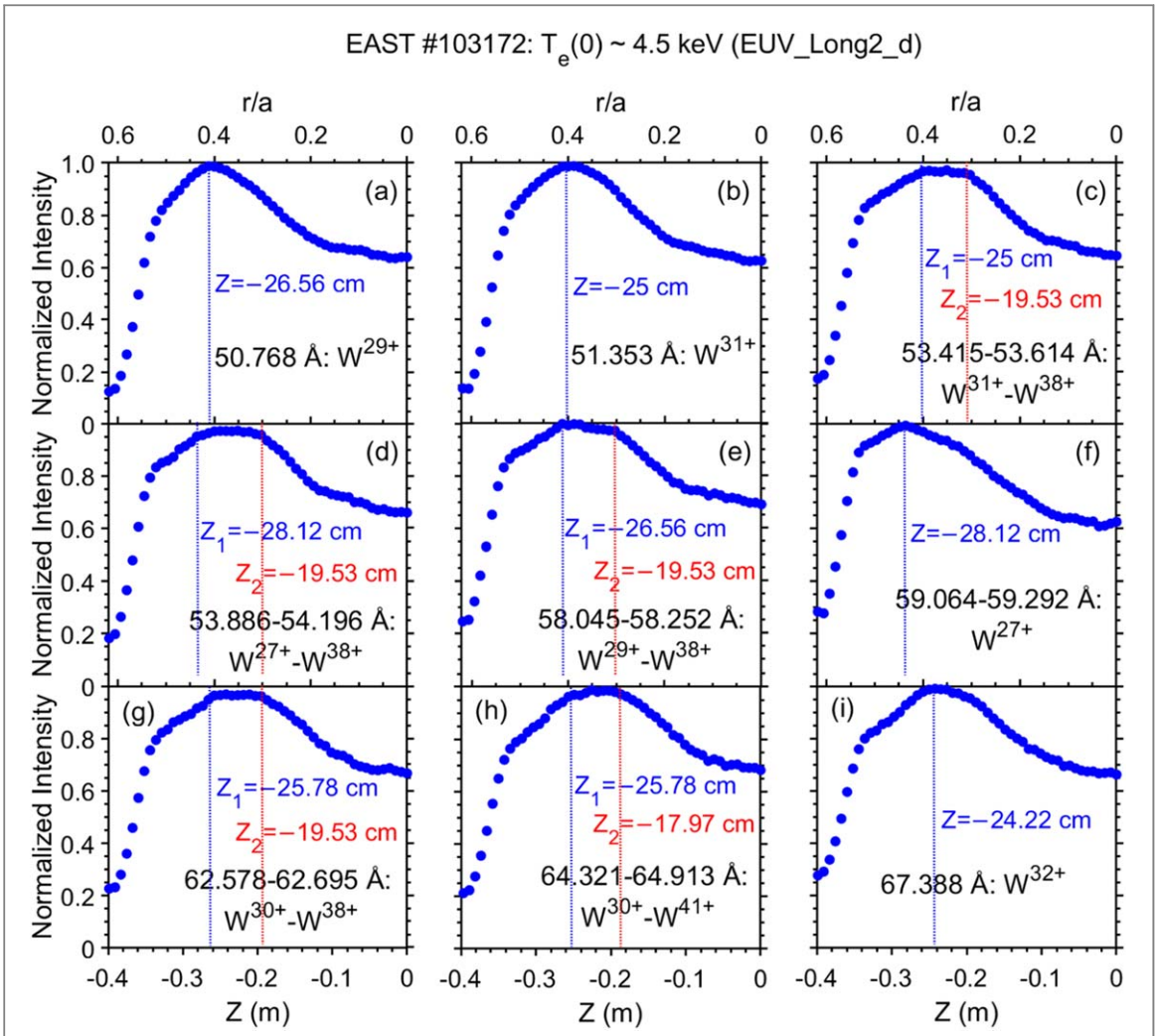

Figure 23. Vertical intensity profiles of unknown tungsten lines at t = 2.476 s during tungsten burst measured with EUV_Long2_d; (a) 50.768 Å: W^{29+}, (b) 51.353 Å: W^{31+}, (c) 53.415–53.614 Å: W^{31+} - W^{38+}, (d) 53.886–54.196 Å: W^{27+} - W^{38+}, (e) 58.045–58.252 Å: W^{29+} - W^{38+}, (f) 59.064–59.292 Å: W^{27+}, (g) 62.578–62.695 Å: W^{30+} - W^{38+}, (h) 64.321–64.913 Å: W^{30+} - W^{41+} and (i) 67.388 Å: W^{32+}. The wavelength interval of unknown tungsten lines is indicated in figure 22. Horizontal axes at the bottom and top indicate plasma vertical position, Z, and normalized minor radius, r/a, respectively (see figures 1 and 13). The intensity is normalized at the peak position. The peak position or peak width is indicated with one or two vertical dotted lines, respectively.

Table 5. Isolated and quasi-continuum tungsten lines newly confirmed in short wavelength range of 50–70 Å. First column gives the wavelengths, λ, determined in this work. Ionization stages estimated from temporal behavior and radial intensity profile are listed in the second column. Third column shows observed intensities. At present transitions are 'unknown' as indicated in the last column. Uncertainty in the wavelength determination is estimated to be 0.01 Å.

λ (Å)	Ionization stages	Intensities (10^{15} phs·m^{-2}·s^{-1}·Sr^{-1})	Transitions
50.768	W^{29+}	0.84	unknown
51.353	W^{31+}	0.71	
53.09–53.216	W^{34+}	0.25	
53.415–53.614	W^{31+} - W^{35+}	0.26–0.28	
53.886–54.196	W^{27+} - W^{35+}	0.25–0.27	
56.811–56.92	W^{30+} - W^{37+}	0.24–0.24	
57.352–57.743	W^{30+} - W^{38+}	0.15–0.16	
58.045–58.252	W^{29+} - W^{38+}	0.17–0.19	
58.686–58.856	W^{30+}	0.18–0.21	
59.064–59.592	W^{27+}	0.17–0.19	
59.71–59.882	W^{27+} - W^{30+}	0.20–0.25	
61.185	W^{38+} - W^{41+}	0.38	
62.578–62.695	W^{30+} - W^{38+}	0.18–0.21	
64.321–64.913	W^{30+} - W^{41+}	0.13–0.18	
67.388	W^{32+}	0.34	
67.811–68.195	W^{32+}	0.06–0.08	

5. Summary

Tungsten spectra in the wavelength range of 10–480 Å were observed in EAST tokamak discharges with tungsten burst events. The observation was done by utilizing four upgraded grazing incidence flat-field fast-time-response EUV spectrometers and two space-resolved EUV spectrometers. EUV spectra at four wavelength ranges of 5–45 Å, 40–180 Å, 130–330 Å and 270–480 Å were simultaneously measured with EUV_Short, EUV_Long_a, EUV_Long_c, and EUV_Long_b spectrometers, respectively. Radial profiles of the tungsten spectra were also observed in the wavelength range of 40–130 Å using EUV_Long2_d spectrometer with function of spatial distribution measurement.

Tungsten lines are examined by comparing the spectra observed before and after the tungsten burst, and identified based on NIST database and previously published data. The tungsten lines identified are re-examined by analyzing the temporal intensity behavior and the radial intensity profile. In all, 213 tungsten lines are found in the spectra after the tungsten burst. The line identification is successfully carried out for 166 tungsten lines, including 78 lines arising from moderately and highly ionized tungsten ions of W^{22+} - W^{45+} in the wavelength range of 10–140 Å and 88 lines arising from low-ionized tungsten ions of W^{4+} - W^{8+} in the wavelength range of 160–480 Å. In other 47 tungsten lines the wavelength or narrow wavelength interval is evaluated in the wavelength range of 50–380 Å and the ionization stages from which the line or wavelength interval arises are determined based on the temporal behavior and the radial profile of tungsten lines. Finally, all tungsten lines studied in this work are summarized in tables. Tungsten lines useful for diagnostics are selected and highlighted in the tables. For example, two strong and isolated W VII lines at 216.351 Å and 261.317 Å and W VIII lines at 197–202 Å can be applied to evaluation of the tungsten influx in fusion experiments. Tungsten UTA spectra in the wavelength of 45–70 Å are useful for evaluation of the tungsten concentration. Isolated W XXV - W XXVII (W^{24+} - W^{26+}) lines at 29–34 Å and W XLIII - W XLVI (W^{42+} - W^{45+}) lines at 60–135 Å can be also used for determining the tungsten density if the radial profile is measured.

The UTA spectrum consisting of quasi-continuum lines is observed in three wavelength ranges for highly ionized and low-ionized tungsten ions, i.e. 18–38 Å for W^{22+} - W^{33+}, 45–70 Å for W^{26+} - W^{45+} and 150–280 Å for W^{5+} - W^{8+}. The tungsten UTA spectra are examined in detail by analyzing the radial profile measured with newly developed EUV_Short2_d spectrometer with CMOS detector, in particular, for the UTA spectrum at 45–70 Å. Finally, the temperature dependence on the UTA spectrum at 140–220 Å is discussed with results from EBIT and other fusion devices. The structural change of the UTA spectrum and the peak shift against the electron temperature observed in this work was very reasonable and well agreed with the EBIT result.

In the near future, the radial profile measurement becomes possible in the full wavelength range of 10–500 Å by installing other space-resolved EUV spectrometers. Further detailed analysis of the tungsten spectra can be expected. In addition, observations of tungsten lines from higher ionization stages of W^{46+} - W^{63+} ions are currently in progress for contributions to ITER diagnosis.

Acknowledgments

This work was supported by the National Magnetic Confinement Fusion Energy R&D Program of China (Grant Nos. 2022YFE03180400, 2022YFE03020004, 2019YFE030403), National Natural Science Foundation of China (Grant No. 12322512), and Chinese Academy of Sciences President's International Fellowship Initiative (PIFI) (Grant Nos. 2025PVA0060, 2024PVA0074).

Data availability statement

All data that support the findings of this study are included within the article (and any supplementary files).

ORCID iDs

Wenmin Zhang https://orcid.org/0009-0000-9980-6765
Ling Zhang https://orcid.org/0000-0001-7880-9588
Yunxin Cheng https://orcid.org/0000-0002-9195-2757
Darío Mitnik https://orcid.org/0000-0003-0193-0958
Haiqing Liu https://orcid.org/0000-0001-6892-358X

References

[1] Neu R, Balden M, Bobkov V, Dux R, Gruber O, Herrmann A, Kallenbach A, Kaufmann M, Maggi C and Maier H 2007 Plasma wall interaction and its implication in an all tungsten divertor tokamak *Plasma Phys. Control. Fusion* **49** B59

[2] Matthews G F *et al* 2009 Current status of the JET ITER-like wall project *Phys. Scr.* **2009** 014030

[3] Luo G N, Liu G H, Li Q, Qin S G, Wang W J, Shi Y L, Xie C Y, Chen Z M, Missirlian M and Guilhem D 2017 Overview of decade-long development of plasma-facing components at ASIPP *Nucl. Fusion* **57** 065001

[4] Bucalossi J, Missirlian M, Moreau P, Samaille F, Tsitrone E, Van Houtte D, Batal T, Bourdelle C, Chantant M and Corre Y 2014 The WEST project: Testing ITER divertor high heat flux component technology in a steady state tokamak environment *Fusion Eng. Des.* **89** 907–12

[5] Chowdhuri M B, Morita S, Goto M, Nishimura H, Nagai K and Fujioka S 2007 Line analysis of EUV spectra from molybdenum and tungsten injected with impurity pellets in LHD *Plasma and Fusion Research* **2** S1060–1060

[6] Pütterich T, Neu R, Dux R, Whiteford A D, O'Mullane M G and ASDEX Upgrade Team, T. 2008 Modelling of measured tungsten spectra from ASDEX Upgrade and predictions for ITER *Plasma Phys. Control. Fusion* **50** 085016

[7] Clementson J, Beiersdorfer P, Magee E W, McLean H S and Wood R D 2010 Tungsten spectroscopy relevant to the diagnostics of ITER divertor plasmas *J. Phys. B: At. Mol. Opt. Phys.* **43** 144009

[8] Harte C S *et al* 2010 Tungsten spectra recorded at the LHD and comparison with calculations *J. Phys. B: At. Mol. Opt. Phys.* **43** 205004

[9] Harte C S, Higashiguchi T, Otsuka T, D'Arcy R, Kilbane D and O'Sullivan G 2012 Analysis of tungsten laser produced plasmas in the extreme ultraviolet (EUV) spectral region *J. Phys. B: At. Mol. Opt. Phys.* **45** 205002

[10] Podpaly Y A, Rice J E, Beiersdorfer P, Reinke M L, Clementson J and Barnard H S 2011 Tungsten measurement on Alcator C-Mod and EBIT for future fusion reactors *Can. J. Phys.* **89** 591–7

[11] Morita S *et al* 2013 A study of tungsten spectra using large helical device and compact electron beam ion trap in NIFS *In AIP Conference Proceedings* **1545** 143–52 American Institute of Physics

[12] Oishi T, Morita S, Huang X L, Zhang H M, Goto M and LHD Experiment Group 2016 Observation of W IV–W VII line emissions in wavelength range of 495–1475 Å in the large helical device *Phys. Scr.* **91** 025602

[13] Liu Y, Morita S, Oishi T, Goto M and Huang X L 2018 Observation of tungsten line emissions in wavelength range of 10-500 Å in large helical device *Plasma and Fusion Research* **13** 3402020–3402020

[14] Dong C F, Morita S, Cui Z Y, Sun P, Zhang K, Murakami I, Zhang B Y, Yang Z C, Zheng D L and Feng L 2019 Evaluation of tungsten influx rate and study of edge tungsten behavior based on the observation of EUV line emissions from W^{6+} ions in HL-2A *Nucl. Fusion* **59** 016020

[15] Oishi T, Morita S, Kato D, Murakami I, Sakaue H A, Kawamoto Y and Goto M 2020 Observation of line emissions from Ni-like W^{46+} ions in wavelength range of 7–8 Å in the Large Helical Device *Phys. Scr.* **96** 025602

[16] Oishi T, Morita S, Kato D, Murakami I, Sakaue H A, Kawamoto Y, Goto M and the LHD Experiment Group 2021 Identification of forbidden emission lines from highly ionized tungsten ions in VUV wavelength range in LHD for ITER edge plasma diagnostics *Nuclear Materials and Energy* **26** 100932

[17] Oishi T, Morita S, Kato D, Murakami I, Sakaue H A, Kawamoto Y, Kawate T and Goto M 2021 Simultaneous observation of tungsten spectra of W^{0} to W^{46+} ions in visible, VUV and EUV wavelength ranges in the large helical device *Atoms* **9** 69

[18] Guirlet R, Desgranges C, Schwob J L, Mandelbaum P, Boumendjel M Y and WEST Team 2022 Extreme UV spectroscopy measurements and analysis for tungsten density studies in the WEST tokamak *Plasma Phys. Control. Fusion* **64** 105024

[19] Cheng Y X, Zhang L, Morita S, Hu A L, Wu Z W, Xu Z, Duan Y M, Xu L Q, Zhong L and Zhang F L 2022 Performance improvement of space-resolved extreme ultraviolet spectrometer by use of complementary metal-oxide semiconductor detectors at the experimental advanced superconducting tokamak *Rev. Sci. Instrum.* **93** 123501

[20] Radtke R, Biedermann C, Schwob J L, Mandelbaum P and Doron R 2001 Line and band emission from tungsten ions with charge 21+ to 45+ in the 45–70- Å range *Phys. Rev.* A **64** 012720

[21] Radtke R, Biedermann C, Mandelbaum P and Schwob J L 2007 X ray and EUV spectroscopic measurements of highly charged tungsten ions relevant to fusion plasmas *In Journal of Physics: Conference Series* **58** 113

[22] Ralchenko Y, Reader J, Pomeroy J M, Tan J N and Gillaspy J D 2007 Spectra of W^{39+}–W^{47+} in the 12–20 nm region observed with an EBIT light source *J. Phys. B: At. Mol. Opt. Phys.* **40** 3861

[23] Clementson J, Lennartsson T and Beiersdorfer P 2015 Extreme ultraviolet spectra of few-times ionized tungsten for divertor plasma diagnostics *Atoms* **3** 407–21

[24] Sugar J and Kaufman V 1975 Seventh spectrum of tungsten (W VII); resonance lines of Hf V *Phys. Rev.* A **12** 994

[25] Iglesias L, Cabeza M I, Rico F R, Garcia-Riquelme O and Kaufman V 1989 The spectrum of doubly ionized tungsten (W III) *J. Res. Nat. Inst. Stand. Technol.* **94** 221

[26] Ryabtsev A N, Kononov E Y, Kildiyarova R R, Tchang-Brillet W Ü L and Wyart J F 2012 $4f^{13}5s^{2}5p^{6}$-$4f^{13}5s^{2}5p^{5}6s$ transitions in the W VIII spectrum and spectra of isoelectronic hafnium, tantalum, and rhenium ions *Opt. Spectrosc.* **113** 109–14

[27] Ryabtsev A N, Kononov E Y, Kildiyarova R R, Tchang-Brillet W Ü L and Wyart J F 2013 The spectrum of seven times ionized tungsten (W VIII) relevant to tokamak divertor plasmas *Phys. Scr.* **87** 045303

[28] Ryabtsev A, Kononov E, Kildiyarova R, Tchang-Brillet W Ü L, Wyart J F, Champion N and Blaess C 2015 Spectra of W VIII and W IX in the EUV region *Atoms* **3** 273–98

[29] Lawson K D *et al* 2022 Observation of low temperature VUV tungsten emission in JET divertor plasmas *Phys. Scr.* **97** 055605

[30] Lawson K D, Pawelec E, Coffey I H, Groth M, Litherland-Smith E, Meigs A G, Scully S and JET Contributors 2015 Determination of tungsten and molybdenum concentrations from an x-ray range spectrum in JET with the ITER-like wall configuration *J. Phys. B: At. Mol. Opt. Phys.* **48** 144023

[31] Utter S B, Beiersdorfer P and Träbert E 2002 Electron-beam ion-trap spectra of tungsten in the EUV *Can. J. Phys.* **80** 1503–15

[32] Das T, Podpaly Y A, Reader J, Gillaspy J D and Ralchenko Y 2018 Analysis of EUV spectra from N-shell tungsten ions observed with an electron beam ion trap *Eur. Phys. J.* D **72** 124

[33] Murakami I, Sakaue H A, Suzuki C, Kato D, Goto M, Tamura N, Sudo S, Morita S and LHD Experiment Group 2015 Development of quantitative atomic modeling for tungsten transport study using LHD plasma with tungsten pellet injection *Nucl. Fusion* **55** 093016

[34] Liu Y, Morita S, Huang X L, Oishi T, Goto M and Zhang H M 2017 Component investigation of ionization stages on tungsten unresolved transition array spectra for plasma diagnostics based on space-resolved extreme-ultra violet spectroscopy in large helical device *J. Appl. Phys.* **122** 233301

[35] Liu Y, Morita S, Murakami I, Oishi T, Goto M and Huang X L 2018 Density evaluation of tungsten W^{24+}, W^{25+}, and W^{26+} ions using unresolved transition array at 27–34 Å in Large Helical Device *Jpn. J. Appl. Phys.* **57** 106101

[36] Drawin H W 1981 Atomic physics and thermonuclear fusion research *Phys. Scr.* **24** 622–55
[37] Kato D *et al* 2013 Observation of visible forbidden lines from highly charged tungsten ions at the large helical device *Phys. Scr.* **2013** 014081
[38] Kato D, Sakaue H A, Murakami I, Goto M, Oishi T, Tamura N, Funaba H and Morita S 2021 Assessment of W density in LHD core plasmas using visible forbidden lines of highly charged W ions *Nucl. Fusion* **61** 116008
[39] Song Y T, Zou X L, Gong X Z, Becoulet A, Buttery R, Bonoli P, Hoang T, Maingi R, Qian J P and Zhong X M 2023 Realization of thousand-second improved confinement plasma with Super I-mode in Tokamak EAST *Sci. Adv.* **9** eabq5273
[40] Zhang W M, Zhang L, Cheng Y X, Morita S, Wang Z X, Hu A L, Zhang F L, Duan Y M, Zhou T F and Wang S X 2022 Line identification of extreme ultraviolet (EUV) spectra from iron, copper and molybdenum ions in EAST tokamak *Phys. Scr.* **97** 045604
[41] Zhang L, Morita S, Xu Z, Wu Z W, Zhang P F, Wu C R, Gao W, Ohishi T, Goto M and Shen J S 2015 A fast-time-response extreme ultraviolet spectrometer for measurement of impurity line emissions in the experimental advanced superconducting tokamak *Rev. Sci. Instrum.* **86** 123509
[42] Zhang L, Morita S, Wu Z W, Xu Z, Yang X D, Cheng Y X, Zang Q, Liu H Q, Liu Y and Zhang H M 2019 A space-resolved extreme ultraviolet spectrometer for radial profile measurement of tungsten ions in the experimental advanced superconducting tokamak *Nucl. Instrum. Methods Phys. Res., Sect. A* **916** 169–78
[43] Li L, Zhang L, Xu Z, Morita S, Cheng Y X, Zhang F L, Zhang W M, Duan Y M, Zang Q and Wang S X 2021 Line identification of extreme ultraviolet (EUV) spectra from low-Z impurity ions in EAST tokamak plasmas *Plasma Sci. Technol.* **23** 075102
[44] Zhang F L, Zhang L, Zhang W M, Cheng Y X, Hu A L, Ding X B, Morita S, Li Z W, Zhou Z and Cao Y M 2024 Line identification of extreme ultraviolet spectra from aluminum ions in EAST Tokamak plasmas *Phys. Scr.* **99** 025615
[45] Kramida A E *et al* 2023 *National Institute of Standards and Technology (NIST)* NIST Atomic Spectra Database (Version 5.11)
[46] Liu H Q, Jie Y X, Ding W X, Brower D L, Zou Z Y, Li W M, Wang Z X, Qian J P, Yang Y and Zeng L 2014 Faraday-effect polarimeter-interferometer system for current density measurement on EAST *Rev. Sci. Instrum.* **85** 11D405
[47] Liu X, Zhao H L, Liu Y, Li E Z, Han X, Domier C W, Luhmann N C, Ti, Jr A, Hu L Q and Zhang X D 2014 Absolute intensity calibration of the 32-channel heterodyne radiometer on experimental advanced superconducting tokamak *Rev. Sci. Instrum.* **85** 093508
[48] Duan Y M, Hu L Q, Mao S T, Xu P, Chen K Y, Lin S Y, Zhong G Q, Zhang J Z, Zhang L and Wang L 2011 Measurement of radiated power loss on EAST *Plasma Sci. Technol.* **13** 546
[49] Zhang L, Morita S, Xu Z, Zhang P F, Zang Q, Duan Y M, Liu H Q, Zhao H L, Ding F and Ohishi T 2017 Suppression of tungsten accumulation during ELMy H-mode by lower hybrid wave heating in the EAST tokamak *Nuclear Materials and Energy* **12** 774–8
[50] Cheng Y X, Zhang L, Morita S, Yang X D, Hu A L, Zhang W M, Zhang F L, Xu Z, Wu Z W and Zang Q 2022 Radial density profiles of highly ionized metallic impurity ions in RF-heated H-mode plasmas in EAST *IEEE Trans. Plasma Sci.* **50** 691–9